People's Democratic Republic of Algeria

Ministry of Higher Education and Scientific Research

University of El Oued

Faculty of Exact Sciences

Laboratory of Operator Theory and Differential Equations

A Doctoral Thesis

Submitted in fulfillment of the requirements for the Doctorate degree in the third cycle (LMD)

Field: Department of Physics

Specialization: Fundamental Physics

Structural, electronic and magnetic properties of FeNi alloys: a DFT study

Presented by: Zineb Zine

Defended in the presence of the Examination Committee:

Name	Rank	Affiliation	Role
Azzeddine Begass	Professor	Echahid Hamma Lakhdar University – El-Oued	**Chair**
Nassima Meftah	Professor	Echahid Hamma Lakhdar University – El-Oued	**Supervisor**
Mourad Mimouni	MCA	Echahid Hamma Lakhdar University – El-Oued	**Examiner**
Abderrahim Achouri	Professor	Kasdi Merbah University-Ouargla	**Examiner**
Lazhar Mahammedi	Professor	Kasdi Merbah University-Ouargla	**Examiner**
Ibrir Miloud	Professor	Mohamed Boudiaf University - M'Sila	**Examiner**

Academic Year: 1446-1447 AH / 2024-2025

Acknowledgments

Above all, I am profoundly grateful to God Almighty for blessing me with the strength, perseverance, and good health that enabled me to complete this work.

I want to express my sincere gratitude to my supervisor, Professor Nassima Meftah, for her invaluable guidance, support, and insightful advice throughout this journey.

I would also like to express my deep appreciation to Professor Faïçal Chemam for his kind assistance and helpful contributions during the course of this research.

My heartfelt thanks are also extended to Professor Azzeddine Begass, Chairman of the committee, for his time, efforts, and valuable consideration.

I would also like to thank the respected examining committee members:

Professor Lazhar Mahammedi,

Professor Abderrahim Achouri,

Professor Mourad Mimouni,

and Professor Ibrir Miloud ,

for their time, remarks, and willingness to evaluate this work...

Dedication

I dedicate this humble work to those who have had a great favor, after God 'ALLAH', in my academic journey,

To my dear mother and father, may God protect them for me, who instilled in me a love of learning and provided me with unlimited support,

To my life partner, who never hesitated to offer me patience and encouragement,

I thank all my family members who have supported and motivated me to persevere,

And to everyone who contributed to the completion of this thesis, even with a word of support or a sincere prayer.

Contents:

Chapter 2: The Theoretical Framework

Chapter 3: Results and Discussions

List of tables:

List of figures:

List of Symbols

Most Commonly Used Abbreviations

$L1_0$ Ordered Tetragonal Structure

Ψ Special Function

$\hat{H}$ System Hamiltonian

$\rho(r)$ Electron Charge Density

E_{XC} Exchange–Correlation Energy

V_{XC} Exchange–Correlation Potential

Tn Nuclear Kinetic Energy

Te Kinetic Energy of Electrons

Uen Electron–Nucleus Coulomb Interaction

Unn Nucleus–Nucleus Coulomb Repulsion

Uee Electron–Electron Coulomb Interaction

TB-mBJ Modified Becke-Johnson Power to Change

GGA Approximation of General Gradients

LDA Approximation of Local Density

k-point in Brillouin Zone

B_0 Bulk Modulus

B' Pressure Derivative of the Bulk Modulus

FP-LAPW Full-Potential Linearized Augmented Plane Wave

RMT Rayon Muffin-Tin

DOS Density of States

E_f Fermi Level

Ms Saturation Magnetization

μ_B Bohr Magneton

Tc Curie Temperature

MCA Magnetocrystalline Anisotropy

ملخص:

تمت دراسة الخصائص البنيوية، الإلكترونية، المغناطيسية، والديناميكية الحرارية لسبائك L1₀-FeNi ونسختها المطعمة بالكوبالت، بهدف التحقق في تأثير الكوبالت كعيوب استبدالية. يهدف هذا البحث إلى استكشاف بدائل مغناطيسية دائمة أكثر كفاءة للتطبيقات المتقدمة. تمت الدراسة ضمن إطار نظرية الكثافة الوظيفية (DFT) ، حيث تم التطعيم في موقعين مختلفين داخل السبيكة الأم: استبدال النيكل (O_{Ni}) و استبدال الحديد (O_{Fe}). أظهرت نتائج ثوابت الشبكة المحسوبة توافقًا ممتازًا مع الدراسات السابقة، كما كشفت حسابات طاقة التكوين أن إضافة الكوبالت تعزز الاستقرار البنيوي للسبيكة. علاوة على ذلك، بينت النتائج أن السبيكة FeNi:Co (O_{Ni}) تتمتع بزيادة كبيرة في العزوم المغناطيسية والمغناطيسية التشبعية (Ms)، بينما في FeNi:Co (O_{Fe})، لوحظ انخفاض طفيف في Ms. أما من الناحية الديناميكية الحرارية، فقد تمت الدراسة باستخدام نموذج ديباي شبه التوافقي، حيث تبين أن تقليل تركيز الكوبالت يؤدي إلى خفض كل من معامل التمدد الحراري الحجمي ودرجة حرارة ديباي. بناءً على هذه النتائج، تعد سبائك FeNi المطعمة بالكوبالت مرشحين واعدين للمغناطيسات الدائمة الخالية من العناصر الأرضية النادرة.

Abstract:

The structural, electronic, magnetic, and thermodynamic properties of L1₀-FeNi alloys and their cobalt-doped counterparts have been investigated to assess the impact of cobalt as substitutional defects. This study aims to explore potential alternatives for more efficient permanent magnets in advanced applications. The research was conducted within the framework of Density Functional Theory (DFT), where doping was performed at two different sites within the parent alloy: nickel substitution (O_{Ni}) and iron substitution (O_{Fe}). The computed lattice parameters showed excellent agreement with previous studies, while the formation energy calculations indicated that cobalt doping enhances the structural stability of the alloy. Furthermore, the results revealed that the FeNi:Co (O_{Ni}) alloy exhibits a significant increase in magnetic moments and saturation magnetization (Ms), whereas FeNi:Co (O_{Fe}) shows a slight decrease in M_s. From a thermodynamic perspective, the study was conducted using the quasi-harmonic Debye model, demonstrating that reducing cobalt concentration leads to a decrease in both the volumetric thermal expansion coefficient and the Debye temperature. Based on these findings, cobalt-substituted FeNi alloys emerge as promising candidates for rare-earth-free permanent magnets.

Résumé:

Les propriétés structurales, électroniques, magnétiques et thermodynamiques des alliages $L1_0$-FeNi et de leurs versions dopées au cobalt ont été étudiées afin d'évaluer l'impact du cobalt en tant que défauts substitutionnels. Cette étude vise à explorer des alternatives potentielles pour des aimants permanents plus efficaces dans des applications avancées. La recherche a été menée dans le cadre de la théorie de la fonctionnelle de la densité (DFT), où le dopage a été réalisé à deux sites différents dans l'alliage d'origine : substitution du nickel (O_{Ni}) et substitution du fer (O_{Fe}). Les paramètres de réseau calculés ont montré un excellent accord avec les études précédentes, tandis que les calculs de l'énergie de formation ont indiqué que le dopage au cobalt améliore la stabilité structurelle de l'alliage. De plus, les résultats ont révélé que l'alliage FeNi:Co (O_{Ni}) présente une augmentation significative des moments magnétiques et de la magnétisation à saturation (Ms), tandis que FeNi:Co (O_{Fe}) montre une légère diminution de Ms. D'un point de vue thermodynamique, l'étude a été réalisée en utilisant le modèle quasi-harmonique de Debye, démontrant qu'une réduction de la concentration en cobalt entraîne une diminution du coefficient de dilatation thermique volumique ainsi que de la température de Debye. Sur la base de ces résultats, les alliages FeNi substitués au cobalt apparaissent comme des candidats prometteurs pour des aimants permanents sans terres rares.

General introduction

General introduction:

Materials used for permanent magnets have gained significant attention due to their crucial roles in modern technological advancements, such as electric motors, data storage devices, and renewable energy systems [1, 2]. The unique properties of hard magnetic materials, including substantial uniaxial magnetic anisotropy, high saturation magnetization, elevated Curie temperatures, coercivity, and high energy products, contribute to their growing importance [3-5]. However, the cost of high-performance permanent magnets is considerably increased because many of them contain rare-earth (RE) elements, such as Pr, Sm, Nd, Tb, or Dy.

The excessive reliance on rare-earth hard magnets has resulted in a concerning depletion of rare-earth elements, despite their numerous advantages. A significant obstacle limiting the broad application of high-performance hard magnets lies in the expensive nature of these raw materials. It is crucial to explore new materials and rare-earth-free alternatives that can rival or even exceed the outstanding performance of rare-earth magnets to tackle these issues.

A significant breakthrough in materials science, the identification and advancement of ordered ternary intermetallic compounds featuring the $L1_0$ structure, holds transformative potential for both fundamental research and real-world applications [6,7]. $L1_0$-FeNi, $L1_0$-FePt, and $L1_0$-CoPt alloys are highly prized for their exceptional mechanical, thermal, and magnetic properties, positioning them as leading candidates for next-generation material innovation [8-10]. The unique atomic arrangement in the tetragonal lattice of $L1_0$ alloys provides them with distinctive magnetic properties, such as high uniaxial magnetic anisotropy, leading to remarkable coercivity and saturation magnetization [11,12]. This capability to sustain stable magnetic domains at reduced scales is vital for the development of high-density magnetic storage technologies. Additionally, owing to their superior performance and sustainability, $L1_0$ alloys could serve as viable alternatives to rare-earth-based magnets. This marks a significant step forward in the pursuit of more economically viable and environmentally sustainable materials.

The $L1_0$-FeNi alloy, that is the tetrataenite phase, is found exclusively in meteorites and forms under conditions of extremely slow cooling, at a rate of approximately 0.1 K per

million years, and a temperature close to 600 K [13]. A recent breakthrough has enabled scientists to successfully synthesize highly ordered tetragonal FeNi alloy in the lab using an innovative and efficient method [14]. The $L1_0$-FeNi alloy displays several notable properties, including a substantial theoretical maximum energy product of (BH)max = 446 kJ/m³, a high saturation magnetization of Ms = 1.5 T, and a relatively elevated Curie temperature of TC = 830 K. It also features exceptional mechanical strength. Furthermore, the L10-FeNi alloy possesses remarkable magnetic characteristics, underscored by its high magnetocrystalline anisotropy (MCA = 1 MJ/m³). However, despite these benefits, the MCA value of L10-FeNi is inadequate for use in permanent magnets [15,16].

The insertion of impurities or defects into materials is referred to as defect engineering. This method offers the potential for improving the structural and magnetic properties of $L1_0$-FeNi alloys. As noted by Rani et al. (2019) [17], the tetragonal distortion caused by substitutional doping with platinum (Pt) significantly affects the magnetocrystalline anisotropy (MCA) of $L1_0$-FeNi. However, Pt doping has proven to be ineffective and fails to produce cost-effective magnets. In contrast, nitrogen (N) doping demonstrates benefits; despite a slight decrease in saturation magnetization, it promotes magnetocrystalline anisotropy and improves the structural rigidity of tetragonally distorted FeNi. This is supported by formation energy calculations of $L1_0$-FeNi with interstitial N-doping [18]. Manchanda et al. [19] studied $L1_0$-FeNi alloys for various doping compositions, including Al, Mn, Cr, V, Ni, S, Ti, P, and B at both substitutional and interstitial sites. Their findings revealed that the anisotropy energy increases from 0.20 meV to 0.89 meV per unity cell while B atoms occupy the interstices in the Ni plane.

Density functional theory is among the most popular theoretical instruments in condensed matter physics and quantum chemistry. It offers an effective alternative for addressing the challenges of many-body systems by focusing on electron density rather than complex wave functions. This approach simplifies calculations and enables accurate simulations through powerful numerical methods. The applications of DFT are diverse, including the study of the electronic structures of solids and the determination of the magnetic properties of certain alloys [20,21].

One of the most prominent computing techniques based on ab-initio principles is the full-potential linear augmented plane wave (FP-LAPW) method. this approach is well-known for its excellent accuracy and capacity to determine a material's physical characteristics, this as

total energy, band structures electronic, and magnetic moments. As a result, it is an effective tool for studying complex materials and predicting their properties.

This thesis focuses on using density functional theory (DFT) to better understand the structural, electrical, and magnetic properties of L10-FeNi tetragonal alloys and how doping affects their performance. The substitutional doping of cobalt (Co) at two distinct sites—the Ni (O_{Ni}) site and the Fe (O_{Fe}) site—is the main focus of the study. Cobalt was chosen because of its chemical affinity and compatible size with FeNi alloys, which are known to form stable structures with a variety of metals.

The linear amplified plane wave (FP-LAPW) approach is used in this work in the context of density functional theory (DFT). The thesis is divided into three chapters following this introduction:

Chapter 1 presents a comprehensive literature review, providing an overview of $L1_0$-FeNi alloys, their applications, and the principles of magnetic materials.

Chapter 2 discusses the basis of density functional theory (DFT) and introduces the ab-initio method (FP-LAPW) that will be used to investigate the properties of the alloys. This chapter also describes the various approximations employed in this research, as well as the Wien2k code.

In Chapter 3, We show the findings of our computations according to the compounds' various characteristics. Finally, the general conclusion provides a summary of the key findings.

References

[1] Hirosawa, S., Nishino, M., & Miyashita, S. (2017). Perspectives for high-performance permanent magnets: applications, coercivity, and new materials. Advances in Natural Sciences: Nanoscience and Nanotechnology, 8(1), 013002.

[2] Tian, L. Y., Levämäki, H., Eriksson, O., Kokko, K., Nagy, Á., Délczeg-Czirják, E. K., & Vitos, L. (2019). Density Functional Theory description of the order-disorder transformation in Fe-Ni. Scientific Reports, 9(1), 8172.

[3] Obeidat, A., Al-Aderah, B., & Qaseer, M. K. (2023). Influence of oxygen and nitrogen doping on the structure and magnetic properties of CoNi alloy: First principle calculations. Journal of Physics and Chemistry of Solids, 172, 111082.

[4] Aladerah, B., & Obeidat, A. (2024). Pressure-dependent magnetic properties of FeNi alloy: Theoretical study. Solid State Sciences, 148, 107437.

[5] Shao, Z., & Ren, S. (2020). Rare-earth-free magnetically hard ferrous materials. Nanoscale Advances, 2(10), 4341-4349.

[6] Laughlin, D. E., Srinivasan, K., Tanase, M., & Wang, L. (2005). Crystallographic aspects of L10 magnetic materials. Scripta Materialia, 53(4), 383-388.

[7] Mandal, S., Debata, M., Sengupta, P., & Basu, S. (2023). L10 FeNi: a promising material for next generation permanent magnets. Critical Reviews in Solid State and Materials Sciences, 48(6), 703-725.

[8] Woodgate, C. D., Patrick, C. E., Lewis, L. H., & Staunton, J. B. (2023). Revisiting Néel 60 years on: The magnetic anisotropy of L10 FeNi (tetrataenite). Journal of Applied Physics, 134(16).

[9] Islam, M., Sarker, M. S. I., Nakamura, T., Khan, M. K. R., Khan, F. A., Islam, M. A., ... & Sato, S. (2021). Structural, electronic and magnetic properties of L10 ordered CoPt nanoparticles: An experimental and DFT study. Materials Chemistry and Physics, 269, 124727.

[10] Aledealat, K., Aladerah, B., Obeidat, A., & Gharaibeh, M. (2021). First-principles study of electronic structure and magnetic properties of L10-ordered FeNi, FePd, and FePt alloys. Heliyon, 7(12).

[11] Vero, K., Islam, R., & Borah, J. P. (2023). First-principles study on the enhancement of structure stability and magnetocrystalline anisotropy energy of L10-ordered Mn1− xFexAlC compound for permanent magnet application. Journal of Applied Physics, 134(15).

[12] Huskisson, D. C. (2018). Structural Characterization of L10 Ordered Materials for Spintronics. The University of Manchester (United Kingdom).

[13] Meftah, N., Mostefaoui, S., Jambon, A., Guedda, E. H., & Pont, S. (2016). Minor and trace element concentrations in adjacent kamacite and taenite in the Krymka chondrite. Meteoritics & Planetary Science, 51(4), 696-717.

[14] Hlova, I. Z., Dolotko, O., Abramchuk, M., Biswas, A., Mudryk, Y., & Pecharsky, V. K. (2024). Enhancement of hard magnetism and chemical order of synthetic L10-FeNi. Journal of Alloys and Compounds, 981, 173619.

[15] Werwiński, M., & Marciniak, W. (2017). Ab initio study of magnetocrystalline anisotropy, magnetostriction, and Fermi surface of L10 FeNi (tetrataenite). Journal of Physics D: Applied Physics, 50(49), 495008.

[16] Lewis, L. H., Mubarok, A., Poirier, E., Bordeaux, N., Manchanda, P., Kashyap, A., ... & Barmak, K. (2014). Inspired by nature: investigating tetrataenite for permanent magnet applications. Journal of Physics: Condensed Matter, 26(6), 064213.

[17] Rani, P., Thakur, J., Taya, A., & Kashyap, M. K. (2019). Magnetocrystalline anisotropy of Pt-doped L10-FeNi compound for clean energy applications. Vacuum, 159, 186-190.

[18] Qiao, Z., Tsujikawa, M., & Shirai, M. (2023). The effect of chemical disorder on magnetic properties of FeNi and Fe2Ni2N alloys. Journal of Magnetism and Magnetic Materials, 568, 170362.

[19] Manchanda, P., Skomski, R., Bordeaux, N., Lewis, L. H., & Kashyap, A. (2014). Transition-metal and metalloid substitutions in L10-ordered FeNi. Journal of Applied Physics, 115(17).

[20] Blaha, P., Schwarz, K., Madsen, G. K., Kvasnicka, D., & Luitz, J. (2001). wien2k. An augmented plane wave+ local orbitals program for calculating crystal properties, 60(1), 155-169.

[21] Weinert, M., Wimmer, E., & Freeman, A. J. (1982). Total-energy all-electron density functional method for bulk solids and surfaces. Physical Review B, 26(8), 4571.

Chapter 1

FeNi alloys

Chapter 1

Physics of FeNi alloys

I.1-Introduction:

Solid magnetic materials have become essential components in various technological applications in recent years. Their unique characteristics, such as high coercive power and large maximum energy products, emphasize their growing significance[1,3]. These properties make hard magnets indispensable in a variety of fields, including magnetic recording media, magneto-optical recording technologies, magnetic sensors, catalytic applications. [4,5].

Among the promising candidates in this field, the $L1_0$-FeNi compound stands out for its exceptional theoretical peak energy product. Also known as tetrataenite, $L1_0$-FeNi is a recently discovered meteoritic mineral with distinctive magnetic properties.

This chapter offers a comprehensive review of the background related to FeNi. It starts with an overview of $L1_0$-FeNi, explores the history of meteorites, after which it talks about the material's magnetic characteristics., highlighting the significance and applications of FeNi alloys.

I.2- Overview of $L1_0$ FeNi alloy(Tetrataenite):

The $L1_0$-FeNi alloy, referred to as the tetrataenite phase, represents a scarce and naturally occurring ordered alloy composed of iron (Fe) and nickel (Ni) that demonstrates a distinctive crystalline arrangement. This alloy is predominantly located within meteorites (Figure (I-1)) and is of significant scientific interest owing to its magnetic characteristics, which exhibit similarities to those of rare-earth magnets.

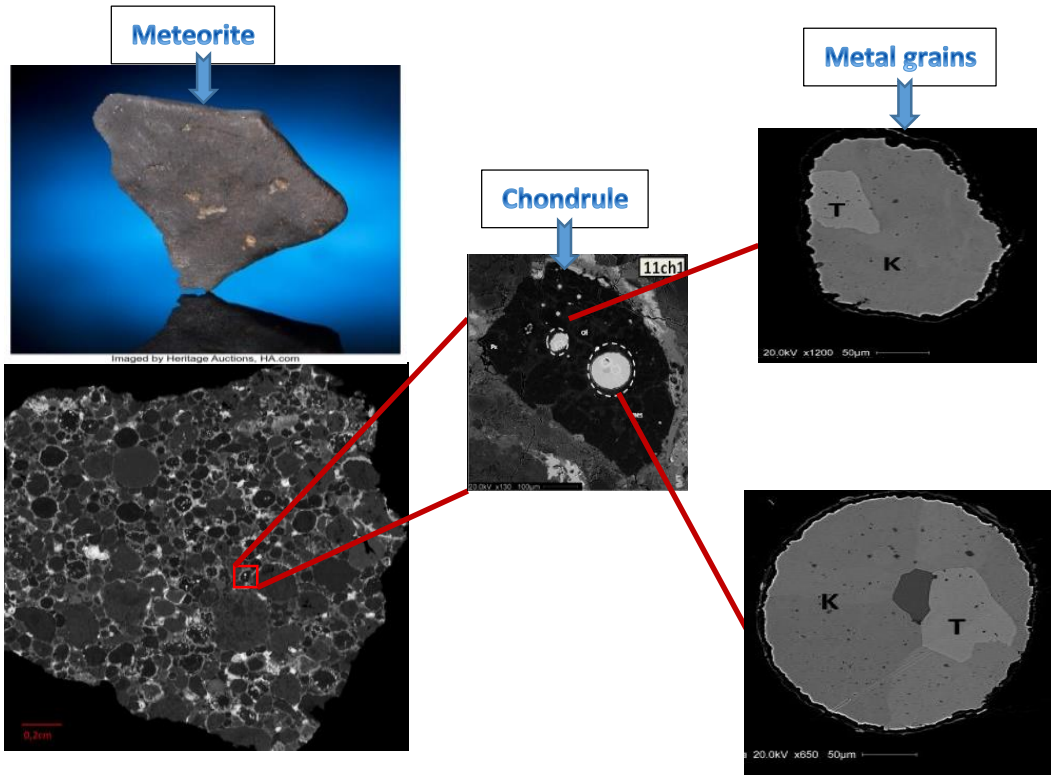

Figure (I-1): BSE image of section of meteorite and its two metal grains. K=Kamacite (FeNi- α) and T= taenite (FeNi- γ) [5].

This alloy is mainly composed of kamacite (containing up to 7% Ni) which has a (body-centered cubic) structure, and the more Ni-rich taenite which has a (face-centered cubic) structure (Figure I-2) with however other elements such as cobalt, tungsten, phosphorus, iridium or chromium [6]. These phases are commonly associated with sulfides (Troilite FeS). The metal grains are included either in the reduced chondrules or isolated in the matrix.

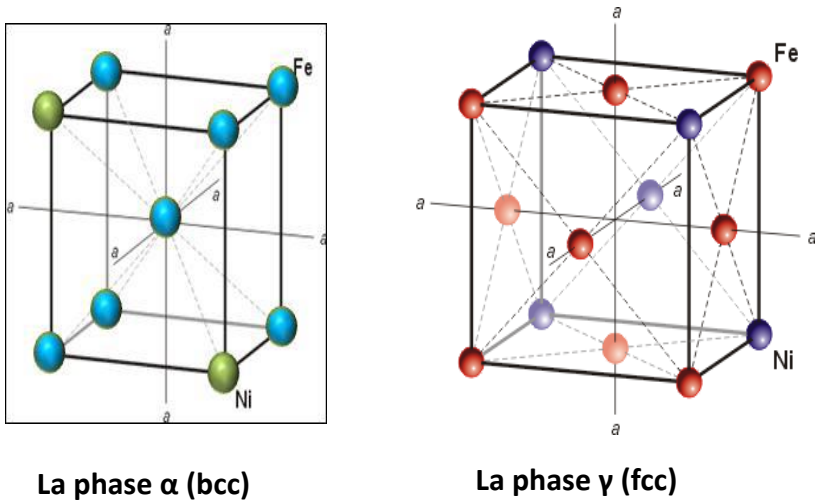

Figure (I-2): The structure of FeNi metallic crystals corresponds to kamacite (the α phase) and taenite (the γ phase).

Thus, meteorites offer a unique window into studying the Fe-Ni system due to their prolonged cooling periods, often spanning billions of years, with cooling rates as low as 0.1 K per million years. This extended timescale facilitates phase transformations at low temperatures despite minimal driving forces [7].

I.3- The formation of FeNi alloy:

According to condensation models, FeNi metal condenses around 1400K, from a gas of solar composition for a pressure of 104 bar, [7, 8], and as indicated by the Yang's Fe-Ni phase diagram (Figure I-3), the Fe-Ni alloy is only composed of taenite (γ) at this temperature up to 850C°. During slow cooling, kamacite (the α phase) develops by nucleation to the detriment of the taenite matrix where the alloy becomes biphasic (α + γ), while this last phase is progressively enriched in Nickel with the decrease in temperature. The study of the structure and composition of the metal grains allows to specify the conditions of thermal metamorphism because the metal is sensitive to the effects of secondary processes. However, upon rapid cooling, taenite transforms without diffusion to a metastable body-centered cubic phase, α2-FeNi, named Martensite.

The genesis of the metal is still controversial, with several scenarios having been proposed [9, 10]. Connelly et al. (2001) assumed that the metal is formed by re-condensation after local evaporation of the metal [11]. Another model suggests that the metal grains are formed by reduction of FeO in silicates by carbon or nebular gas [12]. Hewins et al. (1996) demonstrated that metal grains in chondrites are formed by desulfurization of iron sulfides (FeS) by partial volatilization [13].

Yang and Goldstein published the low temperature Fe-Ni system's phase diagram (Figure I.3) in 1996, making it the most latest and comprehensive diagram available. Here is a description of the phase diagram's main characteristics. A dashed-dot-dotted line, denoting the start temperature (M_{start}), indicates a Martensitic transition. The dashed-dotted line with the label $T_C\gamma$ indicates the A_1 phase's Curie temperature, which varies significantly depending on composition. At 48.8 weight percent Ni and 462 degrees Celsius, a point known as the tricritical point is reached where the magnetic contribution to the free energy causes a miscibility gap.The γ-phase separates into a high Ni content ferromagnetic γ2-phase and a low Ni content paramagnetic γ1-phase below the tricritical point. Dashed lines represent the spinodal and dashed lines represent the miscibility gap. On Yang and Goldstein's phase diagram, the γ"-phase, also known as the $L1_0$, is depicted as a metastable phase that exists on the high Ni content boundary of the miscibility gap. A short horizontal dashed line at TC γ" = 320 °C indicates the key chemical order-disorder temperature of the γ"-phase. Yang and others [14].

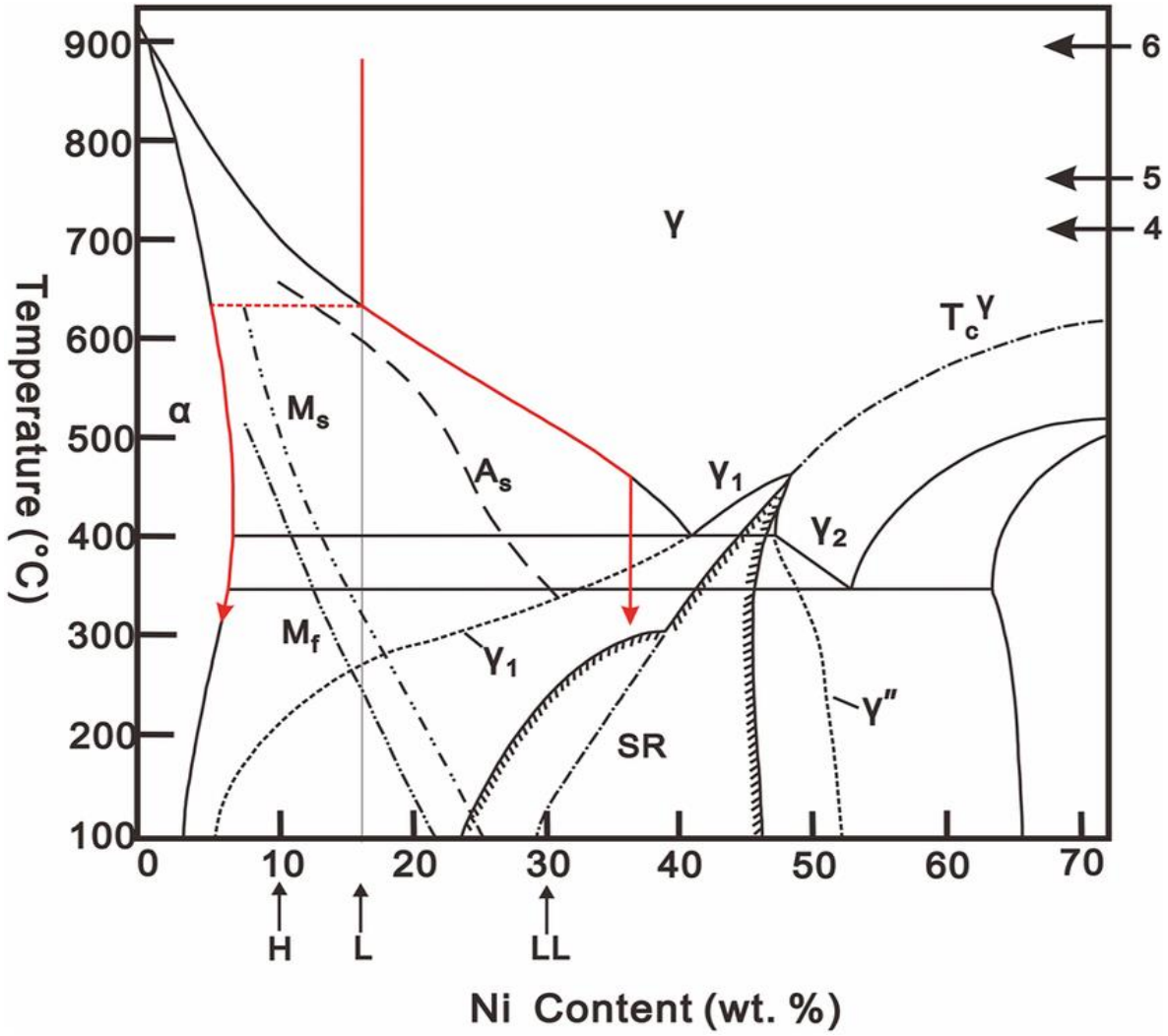

Figure (I.3): Yang's Fe-Ni phase diagram [14].

Particularly observed in some meteorites, terrestrial rocks, and more lately in thin films produced by monatomic layer epitaxial deposition, the synthesis of $L1_0$ FeNi has been detected mainly under specific conditions, such as high-energy electron or neutron irradiation [11].

The importance of electron and neutron irradiation in the formation of $L1_0$-type FeNi was emphasized by early research conducted in the 1960s by Néel and Paulevé et al. The short-range atomic rearrangement that produced the chemically-ordered phase beneath the stated chemical order-disorder temperature of 320 °C was made possible by the introduction of atomic vacancies brought about by these processes. n the latter part of the 1970s, L10 FeNi was identified in the complex microstructures of various slowly-cooled meteorites, providing invaluable insights into the Fe-Ni system's behavior over geological timescales [7].

Although it ignores the existence of readily-formed iron oxides that have peaks similar to those of $L1_0$ FeNi, a recent work that highlights the achievement of $L1_0$ FeNi through extreme plastic deformation offers potential. Efforts towards bulk synthesis on Earth would greatly benefit from a better knowledge of the kinetic mechanisms and energy needs for phase formation [8].

Although research on irradiated and meteoritic samples has investigated the thermodynamic stability of $L1_0$ FeNi (tetrataenite), the question remains open whether L10-type FeNi represents a stability or metastability phase. The chemical order-disorder temperature (TOD) that identifies the structural conversion temperature between FeNi $L1_0$ and A1 phases was established at 320 °C through the examination of neutron-irradiated specimens [11].

These results have been confirmed by later research, which showed that $L1_0$ phase production occurs in Fe-Ni samples that were irradiated between 200 and 400 °C and had initial average compositions ranging from 31 to 70 at% Ni [12].

I.4-The main characteristics of iron and nickel:

We summarize in the following table the most important physicochemical characteristics of Fe and Ni elements:

Table (I.1): The different characteristics of iron and nickel [11].

	Fe	Ni
Electronic structure	[Ar]3d64S2	[Ar]3d84S2
Atomic number (Z)	26	28
Atomic radius (Å)	1.27	1.26
Melting temperature (°C)	1535	1453
Resistivity at 20 °C ($10^{-8}\Omega$.m)	10	7.8
Magnetic state	Ferromagnetic	Ferromagnetic
Curie temperature (C)	770	350
Saturation magnetization Ms (kAm^{-1})	1714	485

I.5-Magnetic properties:

I.5-1 History:

The advent of electrical engineering, more than a century ago now, was accompanied from its beginnings by the development of “magnetic cores” (made of iron) which are at the heart of electromagnetic devices and systems. These “cores” were quickly found combined with silicon (1900s) to reduce “iron losses”; alloyed with cobalt (1920s) to further increase induction, torque and electrical output voltage; alloyed with nickel (1920s) to significantly reduce internal magnetic anisotropies and thus obtain much softer alloys. The large families of crystalline soft magnetic materials emerged in the first half of the 20th century. In the second part of the century, researchers devoted significant research and development efforts to these materials and made major improvements to them thanks to advances in development, metallurgical optimizations of microstructure and usage properties with respect to application needs. In addition to the major case of grain-oriented Fe-Si steels (late 1940s) for distribution transformers, these different families of polycrystalline materials (pure iron, FeSi–Al, Fe–Cr, Fe–Ni, Fe–Co.. .)

mainly limited to direct current or low to medium frequency applications (50 Hz to a few kHz). These soft magnetic materials have been able to adapt throughout the last century to changes in diverse and varied application needs (frequency regime, temperature, energy efficiency, corrosion resistance, mechanical resistance, thermomagnetic resistance to aging, etc.). They continue to evolve today, especially with a view to researching new economical alloys without degrading product performance. The second half of the 20th century will see the emergence of other large families of soft magnetic materials competing with the first wave (crystalline) [15,16].

In the 1950s, soft ferrites arrived and quickly found their way into mass and niche medium and high frequency applications. Then came magnetic amorphous materials in the 1970s, finding their place with difficulty between “crystalline” and ferrites in low-frequency energy transformers, certain passive components, certain sensors, etc. Finally, towards the end of the 1980s, nanocrystalline materials arrived (amorphous/nanocrystal hybrid alloys) very quickly finding their place since the end of the 1990s in specific transformers and inductors. From a metallurgical point of view, this last family (nanocrystals) resulting from amorphous production technology is different from polycrystalline materials produced in ingots or slabs then processed hot and cold. No one (except the Hitachi Metals researchers who were

finishing patenting the birth of this new family) would have bet on making the size of the metallic and ferromagnetic crystals of a crystallized alloy nanometric.

would generate such a combination of excellent magnetic performances while we have been living for almost 100 years with the assurance that the increase in grain sizes rhymes with better magnetic performances (ancestral law) [15-18]

I.5-2 Origin of magnetism:

The phenomenon of material magnetism is the result of the movements of electrons orbiting around the nucleus of atoms. When an electron moves on an orbital, it generates an electric charge in motion that produces a magnetic field. Additionally, as the electron rotates on its axis, known as its spin, it generates yet another magnetic field. The combination of the orbital movement and the spin creates magnetic dipoles that possess a magnetic moment. These magnetic dipoles can be influenced by a magnetic field from the outside [15,19], as shown in Figure (I.4)

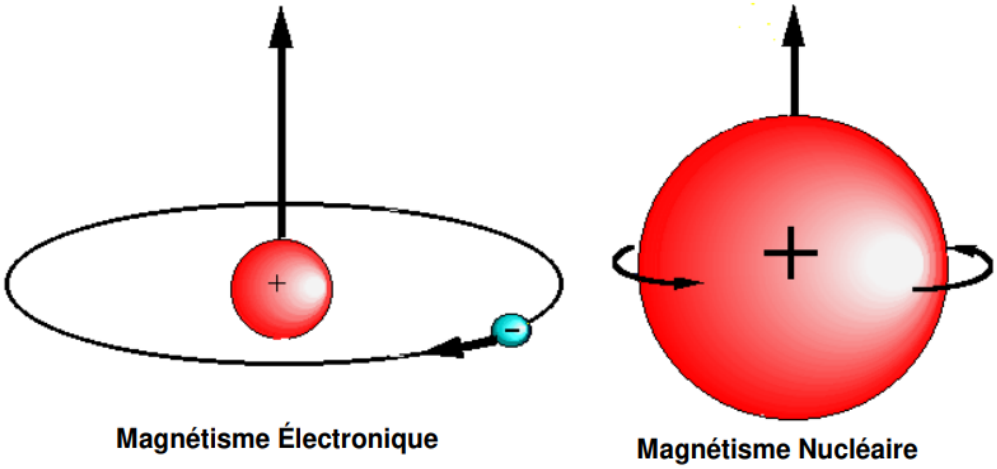

Figure (I-4): Origin of magnetism in matter[10].

The net magnetic moment of the atom is equal to The vector average of the orbital magnetic moments and spins of all the electrons orbiting the nucleus of this atom.

When two electrons are paired, meaning they have opposite spins, their spin magnetic moments are opposite in sign and cancel each other out, so they do not contribute to the overall magnetic moment of the atom. Additionally, the magnetic moment arising from the electrons in any electrical layer or sublayer is zero. As a result, the net magnetic moment of the atom depends solely on the electrons in the outer electronic layers, where the sum of the quantum numbers is not zero [20].

I.5-3 The orbital magnetic moment:

An electron's orbital angular momentum (G_l) as it revolves around an atom's nucleus is linked to its orbital magnetic moment (m_l).Because of the electron's charge, the orbital magnetic moment's direction is opposite to the orbital angular momentum's [19,20].

$$m_l = -\left(\frac{e}{2m}\right) G_l \qquad (I.1)$$

Bohr first proposed the idea that the electron's orbital angular momentum modulus is quantized, or limited to a set of discrete values. To be more precise, Bohr suggested that the electron's orbital angular momentum is a multiple integer of h/2π, where h is Planck's constant.

$$G_L = l\frac{h}{2\pi} \qquad l = 0,1 \ldots\ldots \qquad (I.2)$$

As a result, the magnetic moment m_l is also quantized and must be an integer multiple of a fundamental unit called the Bohr magneton, denoted as μ_B. The Bohr magneton is a fundamental quantity in magnetism and is defined as:

$$G_l = l\mu_B \qquad (I.3)$$

$1\mu_B=9.273.10^{-24}A.m^2$

(this is the unit of magnetic moment on the atomic scale).

I.5-4 The spin magnetic moment:

The spin magnetic moment arises from the intrinsic angular momentum of an electron as it rotates around its own axis, a property known as spin. This concept was first introduced by S.A. Goudsmit and G. Uhlenbeck in 1925 to explain certain features of atomic spectra. The spin angular momentum, denoted by Gs, can take two distinct values, often indicate to as "spin up" and "spin down". These values represent the orientation of the electron's spin relative to an external magnetic field [21,22].

$$G_s = +\frac{1}{2}\left(\frac{h}{2\pi}\right), \quad G_s = -\frac{1}{2}\left(\frac{h}{2\pi}\right) \qquad (I.4)$$

This spin angular moment is associated with a spin magnetic moment such that:

$$m_s = \left(\frac{e}{m}\right) G_s \qquad (I.5)$$

I.5-5 The magnetic moment total:

In atoms that have an incomplete electron subshell, such as the 3d subshell of transition metals and the 4f subshell of rare earth metals, the magnetism is mainly due to electrons. This is because the atomic magnetic moment that comes from the nucleus is typically weaker than the magnetic moment contributed by electrons [22]. When we consider the motion of electrons around the nucleus, we see that the magnetic moment has two main contributions: the orbital contribution (M_L) and the intrinsic angular momentum of the electron, which is known as the spin contribution (spin magnetic moment). Therefore, the total magnetic moment is the combined sum of the orbital and spin moments, expressed as [23]:

$$m = m_l + m_s \qquad (I.6)$$

I.6 Classes of magnetic materials:

The source of magnetism is found in the orbital and spin movements of electrons and their interactions with each other. The optimal way to explain the various types of magnetism is by describing how different materials react to magnetic fields. Surprisingly, all substances possess magnetic properties, although some are significantly more magnetic than others. The primary difference lies in whether there is collective interaction among atomic magnetic moments in the materials. In certain materials, there is no such interaction, while in others, there is a very strong interaction between atomic moments. The magnetic behaviors of materials can be categorized into five major groups [19,24]:

- Diamagnetism
- Paramagnetism
- Ferromagnetism
- Ferrimagnetism
- Antiferromagnetism

I.6-1 Diamagnetism:

Although diamagnetism is sometimes very weak, it is a fundamental property of all matter. This phenomenon arises from the opposing behavior of orbiting electrons when exposed to an external magnetic field. Diamagnetic materials consist of atoms that lack a net magnetic moment, meaning all their orbital shells are filled and there are no unpaired electrons. As a result, a negative magnetization (M) is induced in response to an applied magnetic field (H), leading to a negative magnetic susceptibility (χ). This relationship can be observed by plotting the magnetization (M) against the magnetic field (H) [20,25].

Figure (I.5) illustrates that the magnetization is zero when the magnetic field is zero. Furthermore, the fact that the susceptibility (χ) of diamagnetic materials is independent of temperature (T) is a crucial feature.

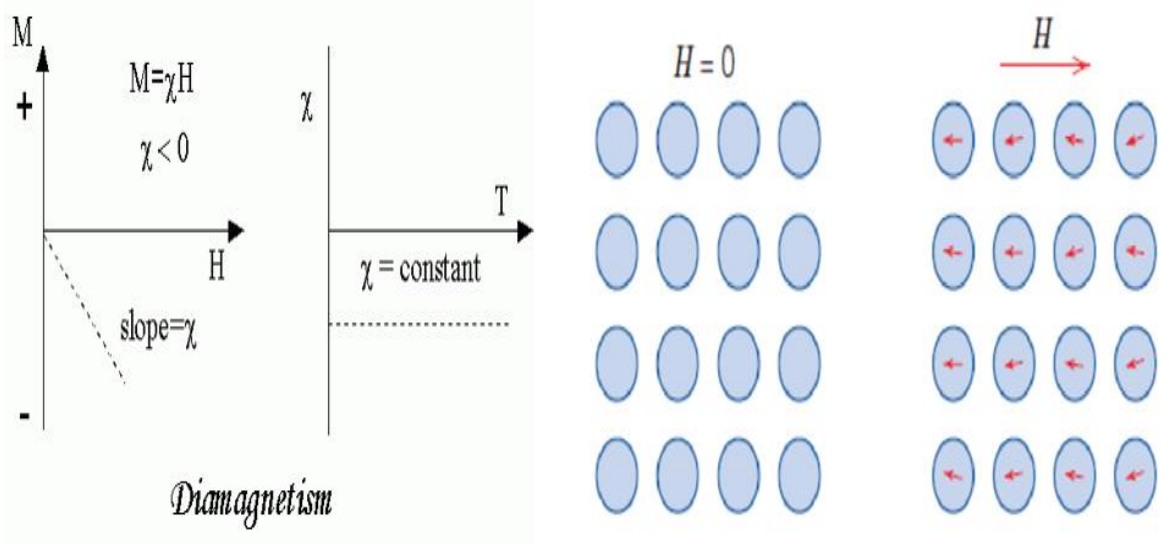

Figure (I.5): The M-H curve, domain alignment (right), and susceptibility (left) are utilized to explain diamagnetism.

I.6-2 Paramagnetism:

Some materials are composed of atoms or ions that exhibit a net magnetic moment because of unpaired electrons located in partially filled orbitals. A notable example of such material is iron, which contains unpaired electrons. In the absence of an external magnetic field, these individual magnetic moments do not interact with each other magnetically, much like in diamagnetic substances, leading to a net magnetization of zero. However, when an external magnetic field is introduced, the atomic magnetic moments partially align in the direction of the applied field. This alignment results in a net positive magnetization and a positive magnetic susceptibility [26], as depicted in Figure (I.6).

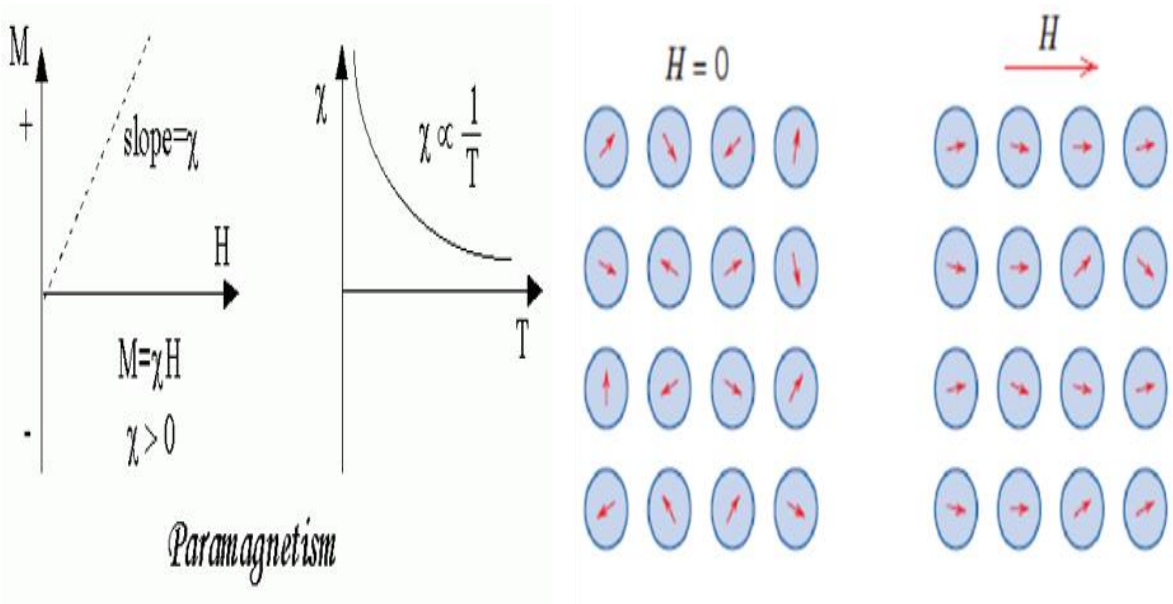

Figure (I.6): M-H curve, susceptibility (left), and domain alignment (right) used to explain paramagnetism.

I.6-3 Ferromagnetism:

These materials exhibit extremely strong interactions between their atomic moments, unlike paramagnetic materials. These interactions, driven by electronic exchange forces, cause the atomic moments to align either parallel or anti-parallel to one another. Exchange forces are exceptionally powerful, being approximately 100 million times stronger than the Earth's magnetic field, equivalent to a field of around 1000 Tesla. The exchange force is a quantum mechanical phenomenon that depends on the relative orientation of the spins of two electrons. In ferromagnetic materials, even in the absence of an external magnetic field, the moments align parallel to each other, leading to a substantial net magnetization [26,27], as illustrated in Figure (I.7).

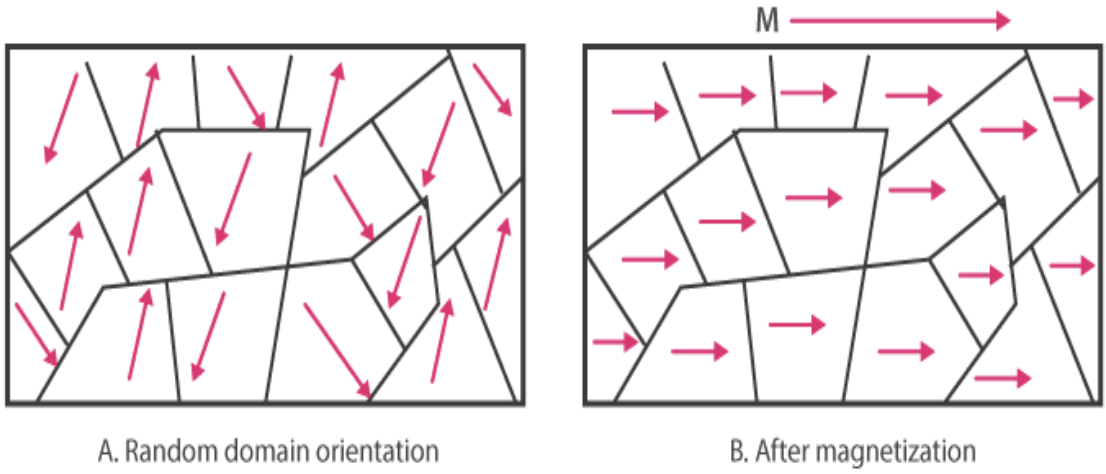

Figure (I.7): Domain alignment in ferromagnetism.

The main ferromagnetic materials include iron, cobalt, nickel, gadolinium, and their alloys. It's worth noting that certain iron alloys are not ferromagnetic, such as the 80% iron, 12% Mn alloy and the 68% Fe 32% Ni alloy which behave like paramagnetic materials. This is also true for all ferromagnetic materials above a so-called "Curie temperature," which is different for each material (for example, Tc for iron is 770°, Ni is 358°, and Co is 1127°). On the other hand, certain alloys such as the 61% Cu, 23.5% Mn, 15% Al alloy are strongly ferromagnetic, while none of the individual constituents have ferromagnetic properties [28].

I.6-3-1 Spontaneous Magnetization:

Spontaneous magnetization is the net magnetization that happens inside a uniformly magnetized tiny volume without the presence of a field. The amount of this magnetization at 0 K depends on the electrons' spin magnetic moments.In the laboratory, the saturation magnetization can be measured,the maximum induced magnetic moment achievable in a magnetic field (Hsat) is referred to as saturation magnetization; beyond this field, magnetization does not increase further. Magnetic domains contribute to the difference between saturation magnetization and spontaneous magnetization. The size of particles does not affect saturation magnetization, which is an inherent characteristic that depends on temperature. The susceptibilities of ferromagnets and paramagnets vary significantly [27,29].

I.6-3- 2 Curie Temperature:

Although ferromagnets possess very strong exchange forces, thermal energy ultimately overcomes the electronic exchange forces, causing a randomizing effect. This occurs at a specific temperature known as the Curie temperature (TC). Consequently, the ferromagnet becomes disordered above this temperature and ordered below the Curie temperature. The saturation magnetization drops to zero when at the Curie temperature. As a diagnostic marker, the Curie temperature is another intrinsic characteristic that could be useful in identifying minerals. However, it is not always reliable, as different magnetic materials may theoretically share the same Curie temperature [20,22].

I.6-3- 3 Hysteresis:

Apart from the saturation magnetization (Ms) and the Curie temperature, ferromagnets are able to recall an applied field even after it has been withdrawn. a phenomenon known as hysteresis is seen in ferromagnetic materials and is defined by a lag between changes in the external magnetic field and changes in the magnetization of the substance. a ferromagnetic material becomes more magnetized when an external magnetic field is applied because the magnetic domains inside the material align with the field's direction.

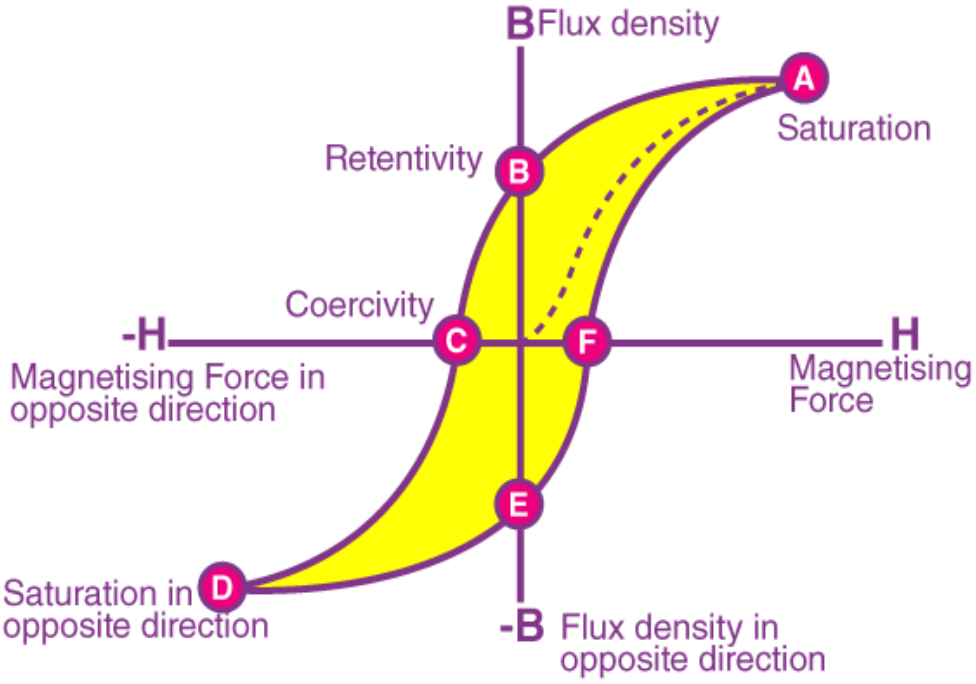

Figure (I.8): Hysteresis Loop.

When the external magnetic field is reduced or removed, the alignment of the magnetic domains does not instantly return to its original state. This delay causes a hysteresis loop when graphing magnetization against the applied magnetic field. Key characteristics shown in the hysteresis loop include coercivity, which is the field required to reduce magnetization to zero, and remanence, which is the magnetization that remains after the external field has been eliminated. Hysteresis is affected by factors such as grain size, temperature, and internal stresses within the material. It plays a crucial role in applications such as magnetic data storage, transformers, and magnetic sensors [19,20].

I.6-4 Ferrimagnetism

Ferrimagnetism is a magnetic phenomenon observed in certain substances. In this phenomenon, the magnetic moments within domains align in an anti-parallel manner, but with different magnitudes. This configuration results in a non-zero total magnetic moment. There are two primary scenarios in ferrimagnetic materials[19-21]:

1. There can be an equal number of crystal sublattices with opposite directions. However, the alignment of magnetic moments in one subassembly may be stronger than in the other. This is seen in materials like ilmenite, magnetite, titanomagnetite, iron oxides, or compounds containing iron and titanium.

2. The number of crystal sublattices aligned in one direction may outnumber those in the opposite direction, as seen in pyrrhotite.

However, ferrimagnetism is temperature-dependent, and it ceases to exist beyond a specific temperature threshold known as the Curie temperature.

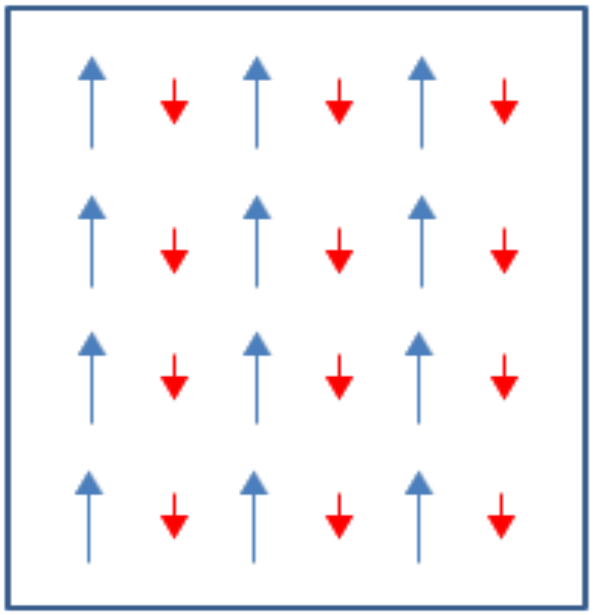

Figure (I.9): Domain alignment in ferromagnetic materials.

I.6-5 Antiferromagnetism:

Although the magnetic moments in antiferromagnetic materials interact with one another, these materials are often composed of two magnetic networks with antiparallel couplings between their magnetic moments [20]. The antiferromagnetic materials do not exhibit macroscopic magnetization because the magnetizations of the two networks balance each other out. Furthermore, as illustrated in Figure I.10, antiferromagnetic materials have a weak, positive susceptibility that varies in a particular manner with temperature, zero remanence, and no hysteresis. Antiferromagnetism depends on the behavior of susceptibility below a threshold temperature, known as the Néel temperature (TN). Above the Néel temperature, susceptibility is governed by the Curie-Weiss law [30,31].

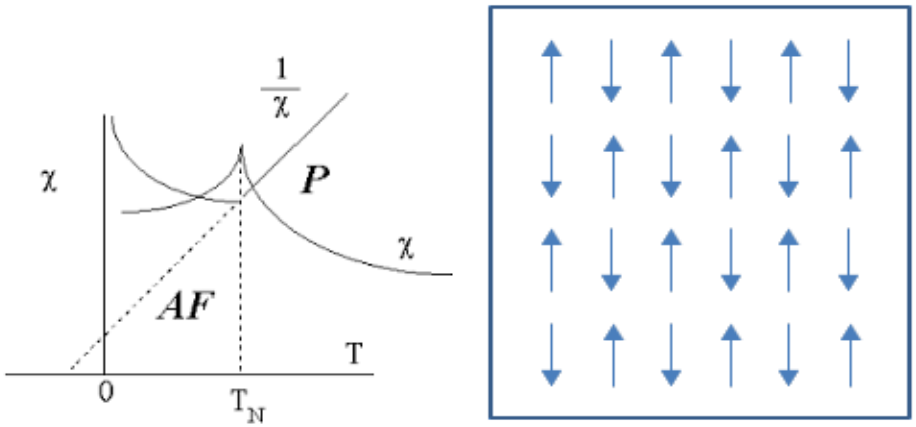

Figure (I.10): Antiferromagnetism's domain alignment (right) and susceptibility as a function of temperature (left).

I.7 Industrial applications of FeNi alloys:

Soft magnetic FeNi alloys are economically significant not because of their high volume use in electrical construction but rather because of their essential function in a variety of devices and components. These alloys serve as the core material for a wide array of devices, including toroids and various other parts. Their significance is especially noticeable in electrically functional and safe equipment. These FeNi alloys provide optimal performance and reliability by enabling the effective functioning of such a wide range of electrical devices[32-35].

The industrial applications of Fe-Ni alloys are diverse and can be categorized into three main types:

I.7-1-Alloys for Miniaturized Electrical Engineering:

Fe-Ni alloys find extensive use in miniaturized electrical engineering applications. They are utilized in various forms such as wires, strips with thicknesses ranging from 0.1 to 2 mm, and grids. These alloys play a crucial role in the construction of compact electrical components, enabling the development of smaller and more efficient devices.

I.7-2-Alloys with Very High Permeabilities:

These alloys are typically manufactured in the form of thin strips and are meticulously treated to enhance their magnetic properties. They are commonly employed in the fabrication of finely tuned circuits where precise control over magnetic flux is essential, contributing to the efficient functioning of electronic devices.

I.7-3-Alloys with Special Hysteresis Cycles:

Fe-Ni alloys with unique hysteresis cycles find specialized applications in the field of electronics, particularly in the development of security devices. These alloys are engineered to exhibit specific magnetic properties that make them suitable for applications requiring controlled magnetization and demagnetization processes. They are integral components in security systems, ensuring reliable performance and accurate detection capabilities.

- **Watchmaking:**

FeNi alloys play a significant role in the prestigious and innovative field of watchmaking. The movement of the hands in classic analog watches is powered by a LAVET-type stepper electric motor. This motor features a bipolar rotor made of a permanent magnet, a stator that is cut from a strip of soft magnetic alloy, and a core that is wound with a possibly different soft magnetic alloy than that of the stator, as shown in (figure-I.11) [34].

Figure (I.11): Electric motor watch of the LAVET type[34].

- **Automotive field:**

Manufacturers in the automotive sector are incorporating an increasing number of sensors and actuators into their products. In the specific area of electric power steering, a torque sensor employs Fe-50%Ni alloy to provide precise measurement of wheel position. Refractory alloys, which are resistant to mechanical wear, oxidation, and high temperatures, are utilized for cylinder head gaskets(figure-I.12) [36,37].

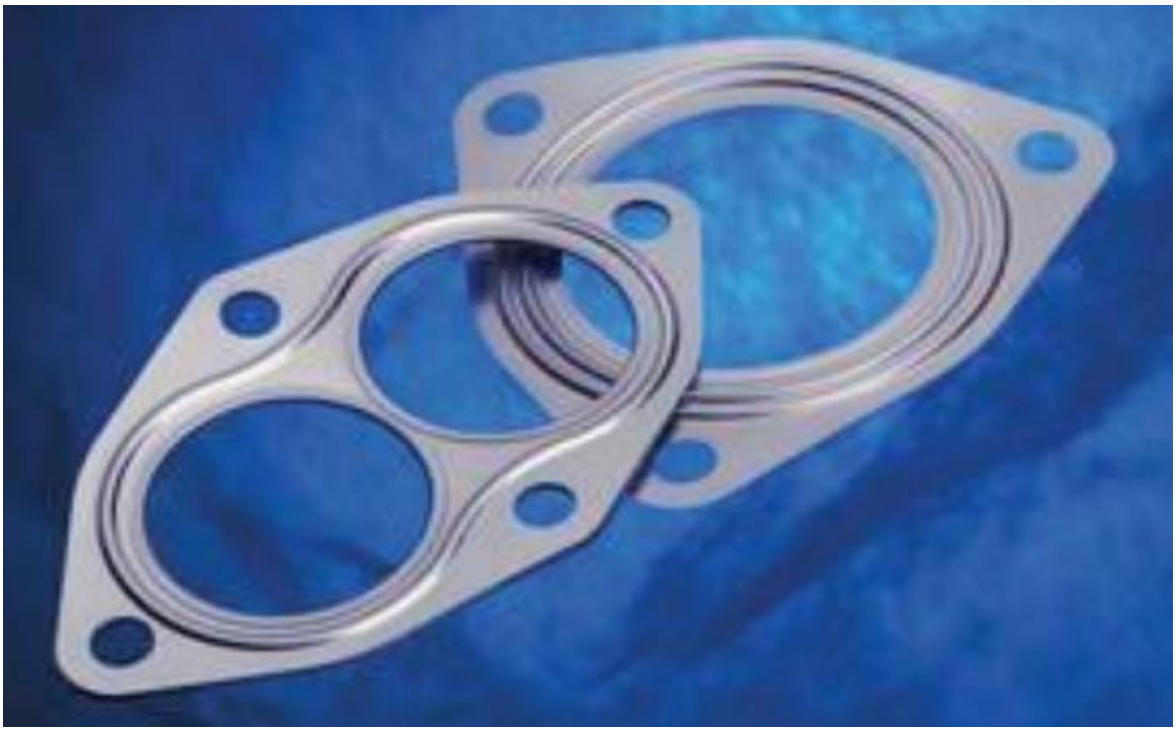

Figure (I.12): Refractory alloys used for gaskets[36].

References:

[1] Hirosawa, S., Nishino, M., & Miyashita, S. (2017). Perspectives for high-performance permanent magnets: applications, coercivity, and new materials. *Advances in Natural Sciences: Nanoscience and Nanotechnology*, *8*(1), 013002.

[2] Tian, L. Y., Levämäki, H., Eriksson, O., Kokko, K., Nagy, Á., Délczeg-Czirják, E. K., & Vitos, L. (2019). Density Functional Theory description of the order-disorder transformation in Fe-Ni. Scientific Reports, 9(1), 8172.

[3] Obeidat, A., Al-Aderah, B., & Qaseer, M. K. (2023). Influence of oxygen and nitrogen doping on the structure and magnetic properties of CoNi alloy: First principle calculations. Journal of Physics and Chemistry of Solids, 172, 111082.

[4] Aladerah, B., & Obeidat, A. (2024). Pressure-dependent magnetic properties of FeNi alloy: Theoretical study. Solid State Sciences, 148, 107437.

[5] Shao, Z., & Ren, S. (2020). Rare-earth-free magnetically hard ferrous materials. Nanoscale Advances, 2(10), 4341-4349

[6] Meftah, N. (2016). Étude chimique et isotopique des alliages métalliques dans les météorites primitives , (Doctoral dissertation, Université Kasdi Merbah Ouargla).

[7] Humayun M., Campbell A. J., Zanda B., and Bourot-Denise M. (2002). Formation of Renazzo chondrule metal inferred from siderophile elements (abstract #1965). 33rd Lunar and Planeraty Science Conference.CD-ROM.

[8] White, W. M. (2013). Trace Elements in Igneous Processes. Geochemistry. John Wiley & Sons.

[9] Wood, J. A. (1963). Physics and Chemistry of Meteorites. Edited by G. P. Kuiper and B. Middlehurts, The University of Chicago Press.

[10] Campbell, A. J., & Humayun, M. (2004). Formation of metal in the CH chondrites ALH 85085 and PCA 91467. Geochimica et Cosmochimica Acta,68(16), 3409-3422.

[11] Connolly, H. C., Huss, G. R., & Wasserburg, G. J. (2001). On the formation of Fe-Ni metal in Renazzo-like carbonaceous chondrites. Geochimica et Cosmochimica Acta, 65(24), 4567-4588.

[12] Zanda, B., Bourot-Denise, M., Perron, C., & Hewins, R. H. (1994). Origin and

metamorphic redistribution of silicon, chromium, and phosphorus in the metal of chondrites. Science, 265(5180), 1846-1849.

[13] Hewins, R. H., Yu, Y., Zanda, B., & Bourot-Denise, M. (1997). Do nebular fractionations, evaporative losses, or both, influence chondrule compositions?.Antarctic meteorite research, 10, 275.

[14] Palme, H., and Jones A. (2005). Meteorites, Comets and Planets: Treatise on Geochemistry, Volume 1, Chapter Solar System Abundances of the Elements, pp. 41. Elsevier.

[15] Néel, L., Pauleve, J., Pauthenet, R., Laugier, J., & Dautreppe, D. (1964). Magnetic properties of an iron—Nickel single crystal ordered by neutron bombardment. Journal of Applied Physics, 35(3), 873-876.

[16] Amblard, J., Maurin, G., & Wiart, R. (1976). Electrocristallisation-Aspects fondamentaux. Techniques de l'Ingénieur D, 906.

[17] Shima, T., Okamura, M., Mitani, S., & Takanashi, K. (2007). Structure and magnetic properties for L10-ordered FeNi films prepared by alternate monatomic layer deposition. Journal of Magnetism and Magnetic Materials, 310(2), 2213-2214.

[18] Paulevé, J., Dautreppe, D., Laugier, J., & Néel, L. (1962). Establishment of an ordered Fe-Ni structure by neutron irradiation. Compt. rend., 254.

[19] Buschow, K. H. J., & Boer, F. R. (2003). Physics of magnetism and magnetic materials (Vol. 7, pp. 11-17). New York: Kluwer Academic/Plenum Publishers.

[20] Wu, C., & Jin, J. (2022). Frontiers in magnetic materials: from principles to material design and practical applications. CRC Press.

[21] Neamţu, B. V. (2010). Matériaux compacts magnétiques doux obtenus à l'état nanocristallin à partir de poudres d'alliages Ni-Fe-X issues de mécanosynthèse (Doctoral dissertation, Université Joseph-Fourier-Grenoble I).

[22] Blundell, S. (2001). Magnetism in condensed matter. OUP Oxford.

[23] Callister Jr, W. D., & Rethwisch, D. G. (2020). Materials science and engineering: an introduction. John wiley & sons.

[24] Cullity, B. D., & Graham, C. D. (2011). Introduction to magnetic materials. John Wiley & Sons.

[25] Pękała, M., Oleszak, D., Jartych, E., & Żurawicz, J. K. (1999). Structural and magnetic study of crystalline Fe80Ni20 alloys with nanometer-sized grains. Journal of non-crystalline solids, 250, 757-761.

[26] Moskowitz, B. M. (1991, June). Hitchhiker's guide to magnetism. In Environmental magnetism workshop (IRM) (Vol. 279, No. 1, p. 48). Univ. of Minn., Minneapolis, Minn: Inst. for Rock Magnetism.

[27] Durand, E. (1968). Magnétostatique. FeniXX.

[28] Chicinaș, I., Pop, V., Isnard, O., Le Breton, J. M., & Juraszek, J. (2003). Synthesis and magnetic properties of Ni3Fe intermetallic compound obtained by mechanical alloying. Journal of alloys and compounds, 352(1-2), 34-40.

[29] Li, H., & Ebrahimi, F. (2003). Synthesis and characterization of electrodeposited nanocrystalline nickel–iron alloys. Materials Science and Engineering: A, 347(1-2), 93-101.

[30]Torabinejad, V., Aliofkhazraei, M., Assareh, S., Allahyarzadeh, M. H., & Rouhaghdam, A. S. (2017). Electrodeposition of Ni-Fe alloys, composites, and nano coatings–A review. Journal of Alloys and Compounds, 691, 841-859.

[31] Clarke, R. S., & Scott, E. R. (1980). Tetrataenite—ordered FeNi, a new mineral in meteorites. American Mineralogist, 65(7-8), 624-630.

[32] Liu, J., & Barmak, K. (2015). Interdiffusion in nanometric Fe/Ni multilayer films. Journal of Vacuum Science & Technology A, 33(2).

[33]Nayak, B., & Meyer, F. M. (2015). Tetrataenite in terrestrial rock. American Mineralogist, 100(1), 209-214.

[34] Kojima, T., Ogiwara, M., Mizuguchi, M., Kotsugi, M., Koganezawa, T., Ohtsuki, T., ... & Takanashi, K. (2014). Fe–Ni composition dependence of magnetic anisotropy in artificially fabricated L1 0-ordered FeNi films. Journal of Physics: Condensed Matter, 26(6), 064207.

[35] Lee, S., Edalati, K., Iwaoka, H., Horita, Z., Ohtsuki, T., Ohkochi, T., ... & Takanashi, K. (2014). Formation of FeNi with L 10-ordered structure using high-pressure torsion. Philosophical magazine letters, 94(10), 639-646.

[36] Yang, C. W., Williams, D. B., & Goldstein, J. I. (1996). A revision of the Fe-Ni phase diagram at low temperatures (< 400 C). Journal of phase equilibria, 17, 522-531.

[37] Béranger, G., Duffault, F., Morlet, J., & Tiers, J. F. (1996). Cent ans apres la découverte de l'Invar... Les alliages de Fer et de Nickel: Technique et Documentation.

Chapter 2

The Theoretical Framework

Chapter 2

The Theoretical Framework

II.1 Introduction:

The behavior of a solid system's electronic structure determines its physical properties, which can be visualized as light electrons circling the heavy nucleus. This has been widely recognized since the advancement of quantum mechanics, which provides the primary concept for these investigations. To fully characterize an N-electron quantum system, the associated wave function, $\Psi(r_1, r_2, r_3,... r_N)$ [1], must be computed. The time-independent Schrödinger equation can be used to derive this in theory, but in reality, each electron's potential is determined by the motion of all the other electrons in the actual system as well as its closest neighbors. This would necessitate solving simultaneous differential equations in a Schrödinger equation. The use of approximations is crucial because, as Dirac noted in 1929 [2], "all progress in this knowledge depends essentially on the development of the most accurate approximation techniques possible". Some theorems, however, address these systems. Hence, the nucleus's motion is merely insignificant since the Born-Oppenheimer approximation views it as a point charge at fixed places. Because the electrons travel swiftly and weigh less than the nucleus, this approximation is rather accurate. Based on this supposition, we can next concentrate our investigation on the electrons because we know they have interactions with the nucleus. Since they can communicate with one another as well, this interaction can be handled even though it cannot be calculated. That means we need to apply different approximations. The bulk of the study on estimating electron-electron interaction in solid systems began in the 1960s, when advances in the understanding of a solid system's electronic structure were made possible by the works of Lu Sham, Walter Kohn, and Pierre Hohenberg. Density functional theory (DFT) is the development of these concepts. Density functional theory's (DFT) primary goal is to use the electron density as a crucial variable in determining a solid system's total energy[3,4]. In this chapter, the theoretical concepts underlying the development of density functional theory, the linearly augmented plane wave (FP-LAPW) approach, and the computer code (WIEN2K) that we employed will all be covered.

II.2 Schrödinger equation:

The Schrödinger equation is one of the basic equations in quantum mechanics. It explains how interacting electrons change over time, which aids in our comprehension of the various physical and chemical characteristics of materials. a solid system consists of nuclei (heavy, positively charged particles) and electrons (light, negatively charged particles).Electrons and nuclei are moving and interacting with one another.This turns into a quantum many-body problem when the particles are so light that quantum mechanics is required. Understanding the behavior of the particles in this system depends on knowing the precise many-particle Hamiltonian [5].

$$H\,\psi = E\,\psi \qquad (II.1)$$

According to the Schrödinger equation, the wave function ψ describes a quantum system's constant state irrespective of time, and H represents the system's Hamiltonian factor, which is expressed as follows:

$$H = T_e + U_{ee} + U_{eN} + T_N + U_{NN} \qquad (II.2)$$

Where,

T_e: Kinetic energy of electrons

U_{ee}: Energy of electron-electron interaction

U_{eN}: Energy of the electron-nucleus interaction

T_N: Kinetic energy of the nuclei

U_{NN}: Nuclei-nuclei interaction energy

As each phrase is developed, we will have:

$$H = -\frac{\hbar^2}{2m_i}\sum_i \nabla_i^2 - \frac{\hbar^2}{2M_\alpha}\sum_\alpha \nabla_\alpha^2 + \frac{1}{2}\sum_{i\neq j}\frac{e^2}{|r_i - r_j|} - \sum_{i,\alpha}\frac{e^2 Z_\alpha}{|r_i - R_\alpha|} + \frac{1}{2}\sum_{\alpha\neq\beta}\frac{e^2 Z_\alpha Z_\beta}{|R_\alpha - R_\beta|} \qquad (II.3)$$

m_i: The mass of the electron i

M_α: The mass of the nucleus α

Z_α: The atomic number of the nucleus α

r_i: The position of the electron i

R_α: The position of the nucleus α

II.3 Fundamental approximations:

II.3-1 Born-Oppenheimer approximation (BOA):

A first-level method for solving multiple-body issues is the Born-Oppenheimer Approximation (BOA), which highlights the significant difference between the mass of the system's electrons (lighter, hence more mobile) and nuclei (significantly heavier M ≈1800 m, so less mobile). To put it another way, this approximation is predicated on the notion that nuclei move slowly enough in relation to electrons for us to ignore them with minimal error, producing a Hamiltonian that is entirely electronic [6].

In this example, the Hamiltonian will be written as follows:

$$H_e = T_e + U_{ee} + U_{eN} \qquad (\text{II. 4})$$

The following is the system's wave equation:

The Born–Oppenheimer approximation only applies when the correlations between the electron motions and the nuclear motions are low, i.e. when the wave function does not change significantly when the nuclei change. Unfortunately, the equation (II.4) has many variables, making direct resolution impossible. Therefore, reasonable approximations must be made.

II.3-2 Hartree-Fock approximation:

Despite the simplifications offered by the Born-Oppenheimer approximation, the presence of N bodies makes it challenging to account for the electron-electron interaction term. When there are more than one electron, solving the Schrödinger equation exactly becomes impossible. In 1927, Douglas Hartree came up with a method to calculate the approximate energies and wave functions of ions and atoms. This approximation is predicated on the idea that electron mobility is uncorrelated and independent of one another [7]. The Hamiltonian for this type of system is expressed as follows:

$$H = \sum_{i=1}^{N_e} h(i) \qquad (\text{II. } 5)$$

Where $h(i)$ is the monoelectronic Hamiltonian.

The exchange interaction is not taken into account in the Hartree approximation. The asymmetry of the wave function when the coordinates of two electrons are switched is what defines this interaction. The following equation can be used to characterize the system with N electrons:

$$\Psi(r_1, \dots r_a, \dots r_b, \dots, r_N) = -\Psi(r_1, \dots r_b, \dots r_a, \dots, r_N) \qquad (\text{II. } 6)$$

The positions of “a” and “b” have been swapped. Ψ (r1, ...,rb, ..., ra, ..., rN) represents the wave function of the N-body system, which is derived from the product of mono-electronic functions. This is because electrons are Fermions (with spin 1/2) and follow a Fermi-Dirac distribution [8].

V. Fock suggested using Slater determinants as an alternative to Hartree’s wave functions. A Slater determinant is an order N determinant composed of N different spin-orbitals, which are mono-electronic functions of spatial and spin variables [9].

The determinant can be represented as follows:

$$\Psi(r_1, r_2, \dots\dots) = \frac{1}{\sqrt{N!}} \begin{vmatrix} \Psi_1(r_1) \dots\dots\dots \Psi_N(r_N) \\ . \\ . \\ . \\ \Psi_1(r_N) \dots\dots\dots \Psi_N(r_N) \end{vmatrix} \quad (\text{II. 7})$$

There is no instantaneous electron-electron interaction because the Hartree-Fock method treats electrons as independent particles moving in a mean potential created by all the nuclei and other electrons; this lack of correlation necessitates the development of specific methods to address this issue.

II.4 Density functional theory (DFT):

The Born-Oppenheimer approximation is used to convert the quantum many-body problem into a system of interdependent electrons subjected to an external nuclear potential, which is still very difficult to solve. Among the various techniques employed to streamline equation (II.4), which effectively characterizes atoms and molecules, the Hartree-Fock method is one of them. However, a more potent approach, known as Density Functional Theory (DFT), stands out as a more contemporary alternative to the Hartree-Fock method. DFT was established in 1964 through the introduction of two theorems by Hohenberg and Kohn. The main idea in this theory is to replace the wave functions with the electronic density function to reduce the number of variables that enter into the calculation [10].

II.4 1-Theorems of Hohenberg and Kohn:

Density functional theory (DFT) is based on two fundamental theorems that were proposed and demonstrated from Hohenberg and Kohn [10,11]:

Theorem 1:

The ground state electron density $\rho(\vec{r})$ and the external potential V_{ext} are established to have a one-to-one connection by the first theorem. Consequently, the total energy of the ground-state system is a special universal function of the electron density.

$$E = E[\rho(r)] \qquad (II.8)$$

Theorem 2:

Hohenberg and Kohn demonstrated that the exact energy of the ground state is represented by this functional minimum value, and that the density corresponding to this energy represents the exact density of the ground state. Additionally, other ground-state properties are determined by this density as well.

$$[\rho_0] = \text{Min}[\rho] \qquad (II.9)$$

ρ_0 the density of the ground state

The properties of a system that are affected by an external potential $V_{ext}(r)$ can all be identified using the electronic density of the ground state.

II.4 2-Kohn-Sham equations:

The Kohn and Sham equations were released in 1965 [12]. these equations are essential, To determine the correlation to exchange contributions for gas of dependent electrons.the difference in kinetic energy functional between an electron gas that is interacting and one that is not is what is known as the correlation energy functional Vc:

$$V_C = T - T_0 \qquad (\text{II. } 10)$$

T denotes the kinetic energy functional of a dependent-electron gas, whereas T0 corresponds to the kinetic energy functional of an independent-electron gas. By comparing the potential energy functional of an interacting and a non-interacting electron gas, the exchange energy functional Vx is obtained.

$$V_x = V - V_H \qquad (\text{II. } 11)$$

where V is a dependent-electron gas's precise potential energy functional and VH represents the Hartree potential energy functional for an independent-electron gas .

This is how the Hohenberg-Kohn functional is expressed.

$$F_{HK} = T + V = T_0 + V_H + V_C + V_x = T_0 + V_H + V_{xc} \qquad (\text{II. } 12)$$

V_{XC} is the energy functional for exchange-correlation.

A representation of the Kohn-Sham Hamiltonian looks like this:

$$\hat{\mathrm{H}}_{KS} = \hat{\mathrm{T}}_0 + \hat{V}_H + \hat{V}_{xc} + \hat{V}_{ext}. \qquad (\text{II. } 13)$$

The functional derivative can be used to determine the exchange-correlation potential:

$$\hat{V}_{xc} = \frac{\delta \hat{V}_{xc}}{\delta p} \qquad (\text{II. } 14)$$

The Kohn and Sham theorem expresses an N-electron system's precise ground-state density

$$\rho(\vec{r}) = \sum_{i=1}^{N} \Phi_i^* (\vec{r}) \Phi_i \overrightarrow{(r)} \qquad (\text{II. } 15)$$

The wave functions for single particles are the N lowest-energy solution of the Kohn Sham equation.

$$\widehat{H}_{KS}\Phi_i = \in_i \Phi_i \qquad (\text{II. } 16)$$

The terms $\hat{V}_H$ and $\hat{V}_{xc}$ are dependent on the density, which in turn is influenced by the Φ_i. The original equation ($\hat{V}_H$ and $\hat{V}_{xc}$ in $\widehat{H}_{KS}$) is dictated by the solves Φ_i, and the equation cannot be represented and solved before its solution is known. This leads to a self-consistency problem. Iterative steps are needed to overcome this paradox.

A guessed density ρ_0 serves as the starting point for this process, from which a Hamiltonian hks1 is constructed. After the eigenvalue problem is resolved, a set of ρ_1 is produced, from which a density can be calculated. The initial rrr0 and calculated rrr1 will typically be different. This ρ_1 is then used to build H_{KS2}, which produces a new value, ρ_2, and so forth. It is possible to build up the technique so that this series will converge to a final density ρ_f that creates an H_{KS2} and yields a solution ρ_f once more. This final density is then consistent with the Hamiltonian.

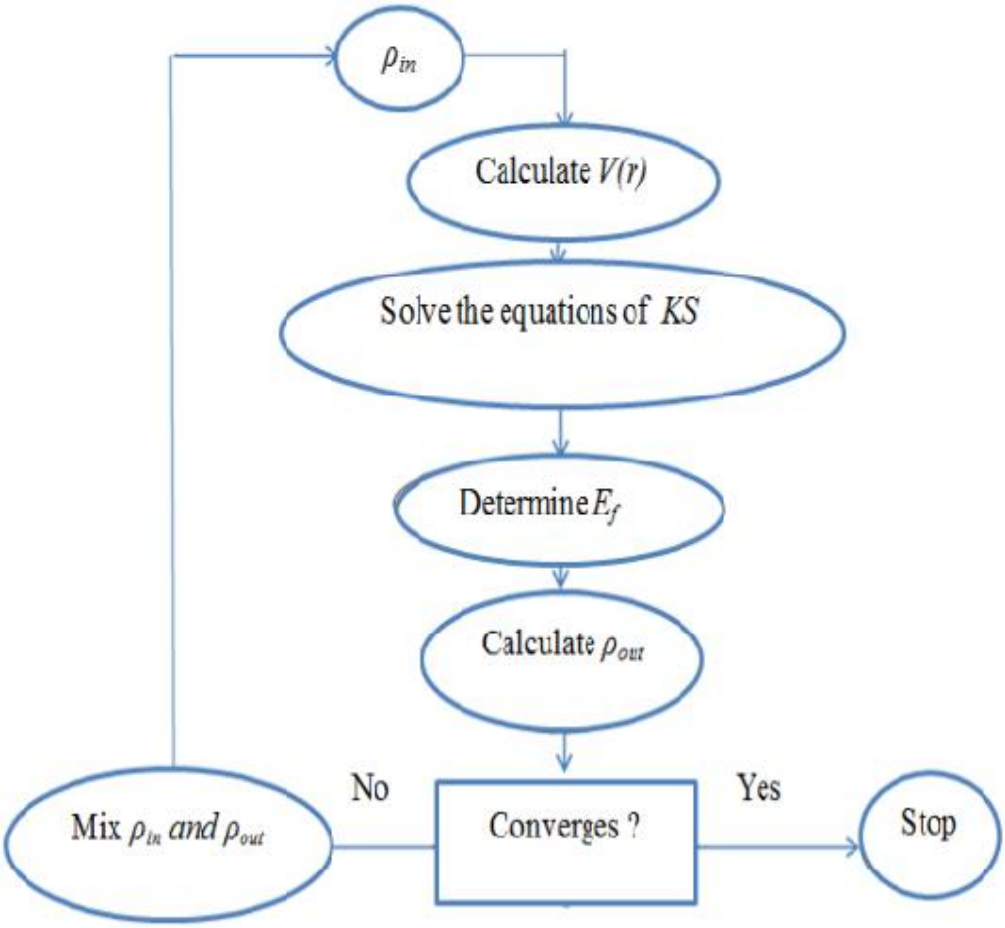

Figure (II.1): Flowchart of the DFT [12].

However, the Kohn-Sham (KS) equations can only be applied when appropriate approximations for the exchange and correlation functional E_{XC} are provided. As a result, various approximations are required to compute the energy and the exchange-correlation potential, with the Local Density Approximation (LDA) and Generalized Gradient Approximation (GGA) being the most prominent ones.

II.4 -3 Approximation of the Local Density (LDA):

The exchange-correlation energy function is approximated $E_{\mathrm{XC}}[\rho]$, The concept of local density approximation (LDA) was suggested by Cohen and Shum in 1965. This approach is predicated on the idea that an electron at a point r in an inhomogeneous electron gas has the same exchange-correlation energy $\mathcal{E}_{XC}[\rho\ (r)]$ as a homogeneous gas with an electron density that is the same as the point density r locally. This is because a gas with an inhomogeneous electron density can be divided into parts of a gas with a uniform density [10, 13].

$$E_{XC}^{LDA}[\rho(r)] = \int [\rho(r)\, \varepsilon_{XC} + \varepsilon_C[\rho(r)] \qquad (\text{II. } 17)$$

II.4 -4 Generalized Gradient Approximation (GGA):

Most of the corrections that have been introduced to the (LDA) are based on the idea of taking into account local variations in the density. For this reason the electron density gradient was introduced leading to the generalized gradient approximations (GGA), in which the exchange and correlation energy are functions of the electron density and its gradient[14]:

$$E_{XC}^{GGA}[\rho, \nabla\rho] = \int \varepsilon_{XC}^{GGA}[\rho(r), |\nabla\rho(r)|]dr \qquad (\text{II. } 18)$$

There are many expressions to describe the GGA functional depending on the choice of ($\rho\ r$, ∇) such as the forms of Becke [15], Perdew and Wang [16] and the most popular, Perdew, Burke and Enzerhoft [17]. Ultimately, the GGA functional gives a lower exchange-correlation energy than the LDA which results in a better agreement with experimental values and generally tends to an overestimation of the lattice parameter and the gap compared to the LDA. However, this improvement is not systematic and it is necessary to compare the results obtained with different approximations and with experimental values when they are available.

II.5 The Linearized Augmented Plane Wave (FP-LAPW) Method:

II.5.1 Introduction:

The study of the different properties of condensed matter is based on various calculation methods, which can be classified into three types: empirical methods, semi-empirical methods, and ab-initio or first principle methods. Density Functional Theory (DFT) is the foundation of a number of ab-initio or first principle techniques. The augmented plane wave (APW) approach was created in 1937 by Slater [18] and subsequently refined by Andersen [19].The modified method is now known as the augmented and linearized plane wave (FP-LAPW) method and is implemented in the new Wien2k calculation code[20]. Before delving into the new method, we will first describe the APW method and the reasons behind the development of the FP-LAPW method.

II.5.2 Augmented Plane Wave (APW) method:

The origin of the idea of Augmented Plane Waves is that, far from the nucleus, electrons can be described by plane waves. This is not the case when they are close to a nucleus. The electron behaves as if it were in an isolated atom. The APW method separated space into two regions[19,21]:

- The first area is captured close to the atomic nucleus, where the wave function and potential resemble those of an isolated atom. The potential in this space, which is bounded by a "Muffin-Tin" (RMT) sphere of radius Rα, is spherical, and the wave functions are radial functions ("solution of the Schrödinger equation").

- The second area is known as the interstitial region (RI), where plane waves are employed as the wave functions and the potential is taken to be constant.

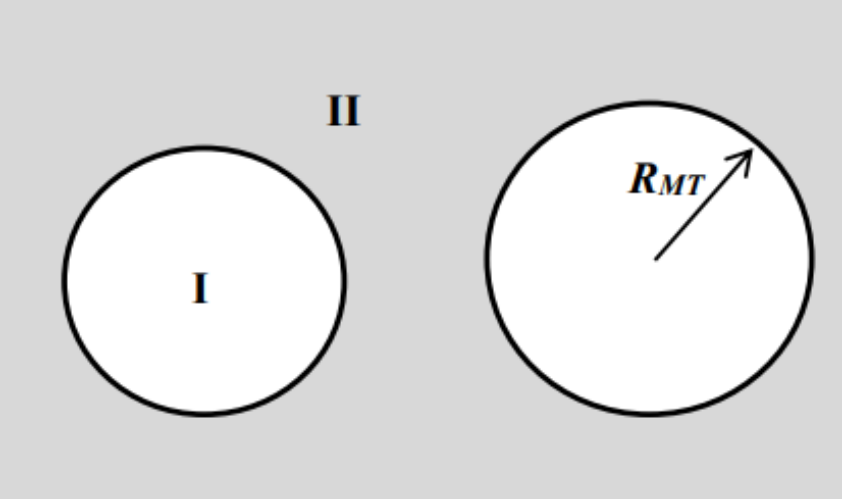

Figure (II.2): Partition of the space using the APW method.

(I): Zone «Muffin-tin», (II): Zone interstitielle[19].

Both the spherical and interstitial regions are defined by the wave functions φ

$$\Phi(r)\begin{cases}\frac{1}{\Omega^{\frac{1}{2}}}\sum_G C_G e^{i(G+K)r} & r > R\alpha \\ \sum_{lm} A_{lm} U_l(r) Y_{lm}(r) & r < R\alpha\end{cases} \qquad \text{(II. 19)}$$

Where:

Rα: is the sphere's radius (MT).

C_G and A_{lm} are the coefficients of the development.

Ω: Volume of the unit cell.

Y_{lm}: The spherical harmonics

The Schrödinger equation involving the radial portion can be regularly solved by the function $U_l(r, E)$, which is expressed as follows:

$$\left\{-\frac{d^2}{dr^2} + \frac{l(l+1)}{r^2} + V(r) - E_l\right\} r U_l(r) = 0 \qquad \text{(II. 20)}$$

Where $V(r)$ is the Muffin-Tin potential and E_l is the linearization energy.

The radial functions, which are orthogonal to any eigenstate of the core and determined by equation (II-21), vanish on the sphere's edge [22]. As demonstrated by the equation that follows:

$$(E_2 - E_1)rU_1U_2 = U_2\frac{d^2rU_1}{dr^2} - U_1\frac{d^2rU_2}{dr^2} \qquad (\text{II.}21)$$

where U_1 and U_2 are radial solutions for energy E_1 and E_2, and the overlap is built by integrating it by parts using equation (II-22), Slater justifies that plane waves are the solution of the Schrödinger equation when the potential is constant, which supports the specific selection of these functions, to ensure the continuity of the function ϕ (r) on the surface of the MT sphere, The following statement represents the coefficients A_{lm}, which must be constructed in terms of the coefficients C_G of the existing plane waves in the interstitial regions.

$$A_{lm} = \frac{4\pi i^l}{\Omega^{1/2}U_l(R_\alpha)}\sum C_G j_l(|K+g|R_\alpha)Y_{lm}^*(K+G) \qquad (\text{II.}22)$$

A_{lm} is determined by the plane wave parameters G_C and the energy parameters E_l. These two terms are variation coefficients in the APW method, as a result, expanded plane waves (APW) are produced when the individual functions, designated G, align with the radial functions of the spheres. Therefore, the energy of the band with index G must equal the energy of E_l. This indicates that the secular determinant must be treated as a function of energy since the energy bands (for a point k) cannot be determined by straightforward diagonalization.

The APW technique has some issues with the function U_l (Rα) that is present in the denominator of equation (III-20). Actually, the value of U_l (Rα) on the M_T sphere's surface can become zero based on the value of the parameter E_l, which causes the radial functions and the plane wave functions to separate. A number of changes have been made to the APW technique to address this issue, most notably those put out by Koelling [23] and Andersen [24]. To create the FP-LAPW approach, the radial functions U_l (r) and their derivatives with respect to the energy U_l are linearly combined to represent the wave function inside the spheres.

II.5.3 Principle of the LAPW method:

According to the LAPW approach [24–26], the MT spheres' basis functions are linear combinations of the radial functions $U_l(r)Y_{lm}(r)$ and their energy-dependent derivatives $\dot{U}_l(r)Y_{lm}(r)$. the U_l functions are defined according to the APW approach, the function $\dot{U}_l(r)Y_{lm}(r)$ must meet the following criteria:

$$\left\{-\frac{d^2}{dr^2}+\frac{l(l+1)}{r^2}+V(r)-E_l\right\}r\dot{U}_l(r)=rU_l(r) \qquad (\text{II.}23)$$

These radial functions $U_l(r)$ and $\dot{U}_l(r)$ guarantee continuity with the plane waves from the outside on the MT sphere's surface in the non-relativistic situation. The wave functions that are augmented in this way become the basis functions (LAPW) of the FP-LAPW approach.

$$\Phi(r)\begin{cases}\frac{1}{\Omega^{\frac{1}{2}}}\sum_G C_G e^{i(G+K)r} & r>R\alpha\\ \sum_{lm}\left[A_{lm}U_l(r)+B_{lm}\dot{U}_l(r)\right]Y_{lm}(r) & r<R\alpha\end{cases} \qquad (\text{II.}24)$$

When the function $\dot{U}_l(r)$ has coefficients B_{lm} that are identical to the coefficients A_{lm}.

As with the APW approach, LAPW functions are plane waves only in interstitial zones; they are more appropriate inside LAPW spheres than APW functions. In fact, a linear combination will duplicate the radial function more accurately than APW functions made up of a single radial function if E_l departs slightly from the band energy El. As a result, the U_l function can be enlarged using its derivative $\dot{U}_l$ and the energy E_l.

$$U_l(E,r)=U_l(E,r)+(E-E_l)\dot{U}_l(r)+0((E-E_l)^2) \qquad (\text{II.}25)$$

Where: $0(E-E_l)^2$ represents the energy squared error.

While the FP-LAPW method produces an error on the wave functions of the order of $(E - El)^2$ and another on the band energies of the order of $(E - El)^4$, the LAPW method thus guarantees the continuity of the wave function on the surface of the MT sphere, but the calculations lose precision in comparison to the APW method, which produces very accurate wave functions. Notwithstanding this order of inaccuracy, the LAPW functions provide a solid foundation that enables the acquisition of every valence band in a wide energy range with just one El. If this isn't feasible, the energy window can usually be split into two sections.Takeda and Kubler [19] proposed an extension of the LAPW method that utilizes N radial functions along with their (N-1) derivatives. This is much more straightforward than the APW approach.

II.5.4 The structure of the calculation:

Numerical simulations now allow us to know the structural and electronic properties of the studied material, among these ab initio methods we have the linear method of augmented plane waves (FP-LAPW) which is used to calculate the electronic structures, this method is introduced in the wien2k code [20]. The Wien2K simulation code was created at the Technical University of Vienna's Institute of Materials Chemistry and released in 1990 by P. Blaha, K. Schwartz, P. Sorintin, and S. B. Trickey [28].

This code has been continually revised in the following years and has undergone several updates. Versions of the original Wien code have been developed (named according to the year of their appearance, Wien93, Wien95, Wien97…). We used the Wien2K version (year 2018). The Wien2K package is written in Fortran, it runs under the LINUX operating system.

It is made up of multiple separate applications linked by C-Shel Script. These applications calculate the electrical structure of solid things using the density functional theory (DFT).
This code can be used to calculate a number of material properties, including:

- Energy bands, state density, and Fermi energy.
- X-ray structural factors, spin density, and electron density.
- Optimizations of structure, equilibrium geometries, atomic forces, and total energy
- Spin polarization (ferromagnetic, antiferromagnetic, or other structure) and spin-orbit coupling.
- X-ray emission and absorption spectra.
- Optical properties

II.6 The Wien2k Algorithm:

The diagram in Figure (II.3) illustrates the development and usage of various Wien2k programs.

The initial step involves running a series of small auxiliary programs that generate inputs for the main programs, known as initialization.

II.6.1- Initialization:

- NN: provides the distances to the closest neighbors and aids in calculating the Muffin-Tin sphere's radius.
- LSTART: specifies how the various orbitals such as core states and valence states, with or without local orbitals, are handled in the band structure computation and generates the atomic densities.
- SYMMETRY: produces the LM expansion for the lattice harmonics, the local rotation matrices, the space group symmetry operations, and the point group of each particular atomic site.

- KGEN: Generates a k-cell in the Brillouin zone.

- DSTART: superimposes the atomic densities produced in LSTART to provide a beginning density for the SCF cycle.

II.6.2- The SCF calculation:

In the second step, we calculate the energy and electron density of the ground state in a self-consistent cycle (SCF). Until the convergence condition is met, this cycle is initiated and continued.The following programs are used for this process:

LAPW0: generates the Poisson potential for density calculation.

LAPW1: computes valence bands, eigenvalues, and eigenvectors.

LAPW2: calculates valence densities for eigenvectors.

LCORE: computes densities and core states.

MIXER: creates a new density by combining core and valence densities.

II.6.3- Calculation of properties:

The following programs are used to calculate physical properties:

- OPTIMISE computes the total energy as a function of volume in order to determine the lattice parameter, compressibility modulus, and its derivative.

- TETRA: calculates the total and partial density of the state.

- SPAGHETTI: uses the eigenvalues produced by LAPW1 to compute the band structure.

- OPTIC: calculates the optical properties.

- XSPEC: determines the X-ray absorption and emission spectrum structures.

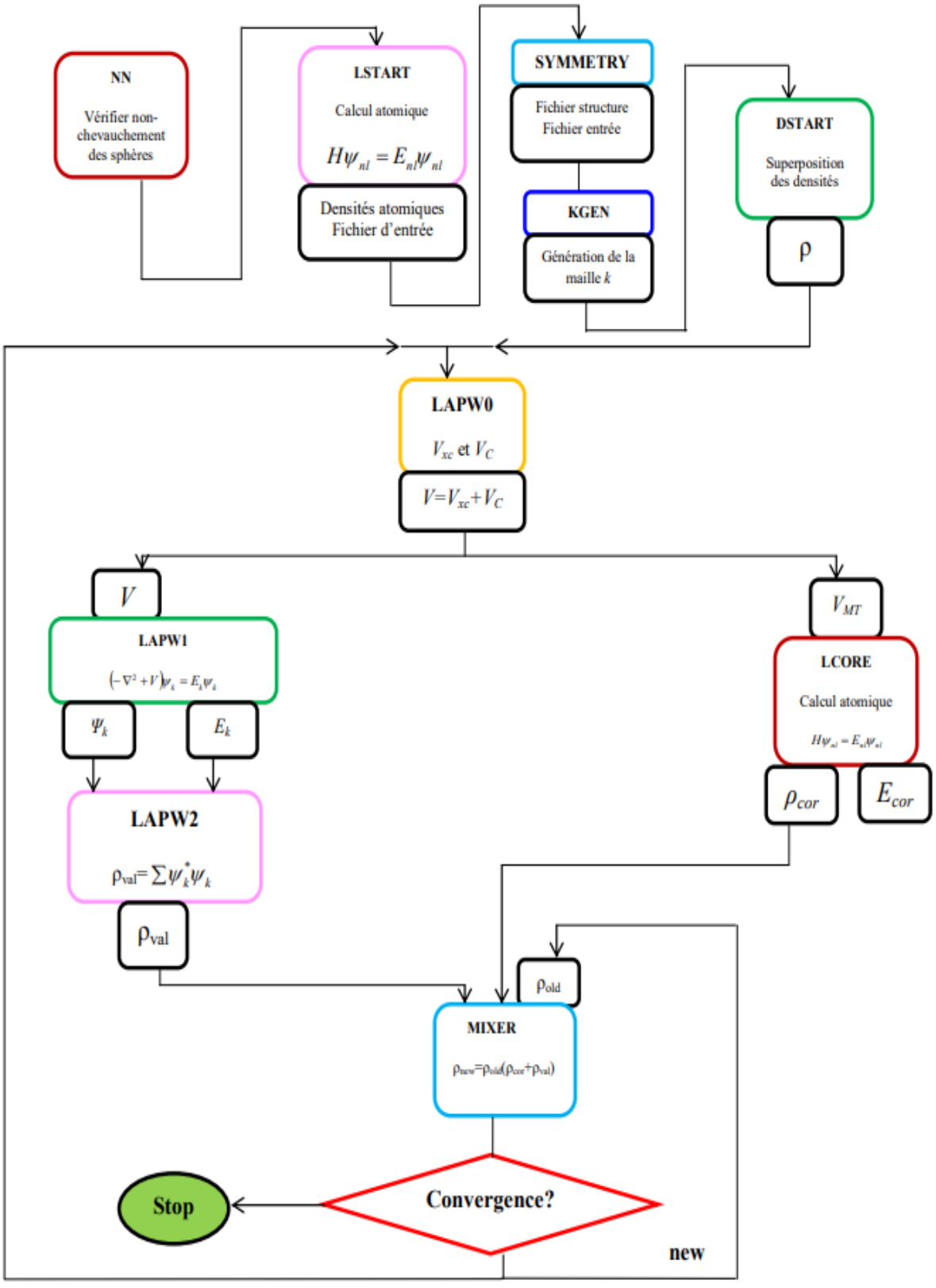

Figure (II.3): The program flowchart of the Wien2K code[28].

References:

[1] Parr, R. G. (1989). Density functional theory of atoms and molecules. In Horizons of Quantum Chemistry: Proceedings of the Third International Congress of Quantum Chemistry Held at Kyoto, Japan, October 29-November 3, 1979 (pp. 5-15). Dordrecht: Springer Netherlands.

[2] Dirac, P. A. M. (1929). Quantum mechanics of many-electron systems. Proceedings of the Royal Society of London. Series A, Containing Papers of a Mathematical and Physical Character, 123(792), 714-733.

[3] Kaltsoyannis, N., & McGrady, J. E. (Eds.). (2004). Principles and applications of density functional theory in inorganic chemistry II (Vol. 2). Springer Science & Business Media.

[4] Iqbal, M. A., Ashraf, N., Shahid, W., Afzal, D., Idrees, F., & Ahmad, R. (2021). Fundamentals of density functional theory: Recent developments, challenges and future horizons. Density Functional Theory-Recent Advances, New Perspectives and Applications.

[5] Schrödinger, E. (1926). Quantisierung als eigenwertproblem. Annalen der physik, 385(13), 437-490.

[6] Born, M.; & Oppenheimer, R ; Zur Quantentheorie der Molekeln. Annalen der Physik, 389, 457-484, (1927)

[7] Hartree, D. R. (1928, January). The wave mechanics of an atom with a non-Coulomb central field. Part I. Theory and methods. In Mathematical Proceedings of the Cambridge Philosophical Society (Vol. 24, No. 1, pp. 89-110). Cambridge university press.

[8]Fermi, E. (1928). Eine statistische Methode zur Bestimmung einiger Eigenschaften des Atoms und ihre Anwendung auf die Theorie des periodischen Systems der Elemente. Zeitschrift für Physik, 48(1), 73-79.

[9] Fock, V. (1930). Näherungsmethode zur Lösung des quantenmechanischen Mehrkörperproblems. Zeitschrift für Physik, 61, 126-148.

[10] Hohenberg, P., & Kohn, W. (1964). Inhomogeneous electron gas. Physical review, 136(3B), B864.

[11] Dirac, P. A. (1930, July). Note on exchange phenomena in the Thomas atom. In Mathematical proceedings of the Cambridge philosophical society (Vol. 26, No. 3, pp. 376-385). Cambridge University Press.

[12] Kohn, W., & Sham, L. J. (1965). Self-consistent equations including exchange and correlation effects. Physical review, 140(4A), A1133.

[13] Perdew, J. P. (1986). Density-functional approximation for the correlation energy of the inhomogeneous electron gas. Physical review B, 33(12), 8822.

[14] Kurth, S., Perdew, J. P., & Blaha, P. (1999). Molecular and solid-state tests of density functional approximations: LSD, GGAs, and meta-GGAs. International journal of quantum chemistry, 75(4-5), 889-909.

[15] Becke, A. D. (1988). Density-functional exchange-energy approximation with correct asymptotic behavior. Physical review A, 38(6), 3098.

[16] Perdew, J. P., & Wang, Y. (1992). Accurate and simple analytic representation of the electron-gas correlation energy. Physical review B, 45(23), 13244.

[17] Perdew, J. P., Burke, K., & Ernzerhof, M. (1996). Generalized gradient approximation made simple. Physical review letters, 77(18), 3865.

[18] Slater, J. C. (1937). Wave functions in a periodic potential. Physical Review, 51(10), 846.

[19] Andersen, E. O., & Jepsen, O. (1977). Advances in the theory of one-electron energy states. Physica B+ C, 91, 317-328.

[20]Blaha, P. (1990). WIEN97, Vienna University of technology 1997. Comput. Phys. Commun., 59, 399.

[21] Slater, J. C., & Phillips, J. C. (1974). Quantum theory of molecules and solids vol. 4: the self-consistent field for molecules and solids. Physics Today, 27(12), 49-50.

[22] Sjöstedt, E., Nordström, L., & Singh, D. J. (2000). An alternative way of linearizing the augmented plane-wave method. Solid state communications, 114(1), 15-20.

[23] Koelling, D. D., & Arbman, G. O. (1975). Use of energy derivative of the radial solution in an augmented plane wave method: application to copper. Journal of Physics F: Metal Physics, 5(11), 2041.

[24] Andersen, O. K., Madsen, J., Poulsen, U. K., Jepsen, O., & Kollar, J. (1977). Magnetic ground state properties of transition metals. Physica B+ C, 86, 249-256.

[25] Singh, D. J., & Nordstrom, L. (2006). Planewaves, Pseudopotentials, and the LAPW method. Springer Science & Business Media.

[26] Shaughnessy, D. J., Evans, G. R., & Darby, M. I. (1987). An improved LAPW method for the calculation of self-consistent electronic band structures. Journal of Physics F: Metal Physics, 17(8), 1671.

[27] Takeda, T., & Kubler, J. (1979). Linear augmented plane wave method for self-consistent calculations. Journal of Physics F: Metal Physics, 9(4), 661.

[28] Blaha, P., Schwarz, K., Madsen, G. K., Kvasnicka, D., & Luitz, J. (2001). wien2k. An augmented plane wave+ local orbitals program for calculating crystal properties, 60(1).

Chapter 3

Results and Discussions

Chapter 3

Results and Discussions

III.1-Introduction:

Permanent magnets play a significant role in many modern technologies, including electric motors, generators, sensors, and data storage devices. The performance of permanent magnets is essentially governed by their magnetic properties, including coercivity, remanence, and maximal energy product [1,2]. Among the materials of interest,the ordered tetragonal FeNi alloy, commonly referred to as $L1_0$-FeNi or tetrataenite, is receiving widespread attention in the materials research community because of its promising magnetic characteristics, which are crucial for advanced technological applications. $L1_0$-FeNi has a unique tetragonal structure, which contributes to its exceptional magnetic properties[3,4]. To better understand and optimize these properties, first-principles calculations based on Density Functional Theory (DFT) provide an effective framework for investigating the structural, electronic, magnetic, and thermodynamic behavior of such alloys [3].

In this chapter, the structural, electronic, magnetic, and thermodynamic properties of the tetrataenite $L1_0$-FeNi alloy are investigated using density functional theory (DFT). This study employs the full relativistic full-potential augmented plane wave plus local orbitals (FPLAPW) method as implemented in the WIEN2K package [6].

III.2-Calculation details:

Density Functional Theory (DFT) was employed to investigate the structural, electronic, magnetic, and thermodynamic properties of the tetrataenite $L1_0$-FeNi alloy. The calculations were carried out using the fully relativistic full-potential linearized augmented plane wave plus local orbitals (FPLAPW) method, as implemented in the **WIEN2k** package [6]. We used GGA+U (Hubbard potential) and spin-polarized GGA, which were created by Perdew, Becke, and Ernzerhof (PBE) [7], for the exchange-correlation energy. The valence levels were handled as scalar relativistically in FPLAPW computations, while the core states were treated fully relativistically. Additionally, the Muffin-tin sphere's valence electronic wave functions were expanded to $l_{max} = 10$. Charge leakage was prevented by selecting the Muffin-tin sphere (R_{MT}) radii for the Fe and Ni atoms in a way that resulted in nearly touching spheres. The plane wave cut-off parameters were found to be $R_{MT}k_{max} = 7$, where R_{MT} is the lowest atomic sphere radius and Kmax is the magnitude of the biggest K vector in the plane-wave expansion. This allowed for the exchange and correlation potential. n the interstitial region, the Fourier expansion of potential has a G_{max} of 12 a.u.$^{-1}$. A dense 6x6x4 k-mesh was utilized to guarantee excellent resolution for computations. The threshold for energy convergence was established at 10^{-4} Ryd. This study employed the quasi-harmonic Debye model with the Gibbs2 computational program to investigate the thermodynamic properties of $L1_0$-FeNi alloy [8, 9]. A function of the crystal's volume can be used to express the Debye temperature using the Voigt Reuss approximation [10]:

$$\Theta = \frac{\hbar}{K}\left[6\pi^2 V^{\frac{1}{2}} n\right]^{\frac{1}{3}} f(\sigma)\sqrt{\frac{B_S}{M}} \qquad \text{(III.1)}$$

M stands for molecular weight per unit of formula, n for number of atoms per unit of formula, B_S for adiabatic bulk modulus, and σ for Poisson ratio [11]. The following is one way to formulate the equation for f(σ) [12] and BS [13]:

$$B_s \simeq B(V) = V\left(\frac{d^2E(V)}{dV^2}\right) \qquad \text{(III.2)}$$

The total energy of the crystal at 0K is expressed as E(V) as a function of volume V.

$$f(\sigma) = \left\{3\left[2\left(\frac{2}{3}\frac{(1+\sigma)}{(1-2\sigma)}\right)^{\frac{3}{2}} + \left(\frac{1}{3}\frac{(1+\sigma)}{(1-\sigma)}\right)^{\frac{3}{2}}\right]^{-1}\right\}^{\frac{1}{3}} \quad \text{(III.3)}$$

These definitions apply to the constant volume heat capacity C_v, the volumetric thermal expansion coefficient α, and the isothermal bulk modulus B_T:

$$B_T(P,T) = V\left(\frac{\partial^2 G^*(V;P,T)}{\partial V^2}\right)_{P,T} \quad \text{(III.4)}$$

$$C_V = 3nk\left(4D(\Theta/T) - \frac{3\Theta/T}{e^{\Theta/T}-1}\right) \quad \text{(III.5)}$$

G* is the Gibbs free energy in non-equilibrium.

D(Θ/T) is the Debye integral

$$\alpha = \frac{\gamma C_V}{B_T V} \quad \text{(III.6)}$$

III.3 Study of Structural, Electronic, Magnetic, And Thermodynamic Properties Of $L1_0$-FeNi Alloy.

III.3-1 Structural properties:

The two types of unit cells that make up the $L1_0$-FeNi crystal structure are (a) face-centered tetragonal (fct) and (b) body-centered tetragonal (bct), as shown in Figure (III.1). The primordial unit cell, or body-centered tetragonal, is frequently employed for computing operations because of its minimum basis, which lowers computational costs [14]. In this work, We examined the bct unit cell, where FeNi crystallizes in an L_{10} tetragonal form with alternating Ni and Fe layers. In this case, the positions of the Fe and Ni atoms are (0, 0, 0) and (0.5, 0.5, 0.5), respectively.

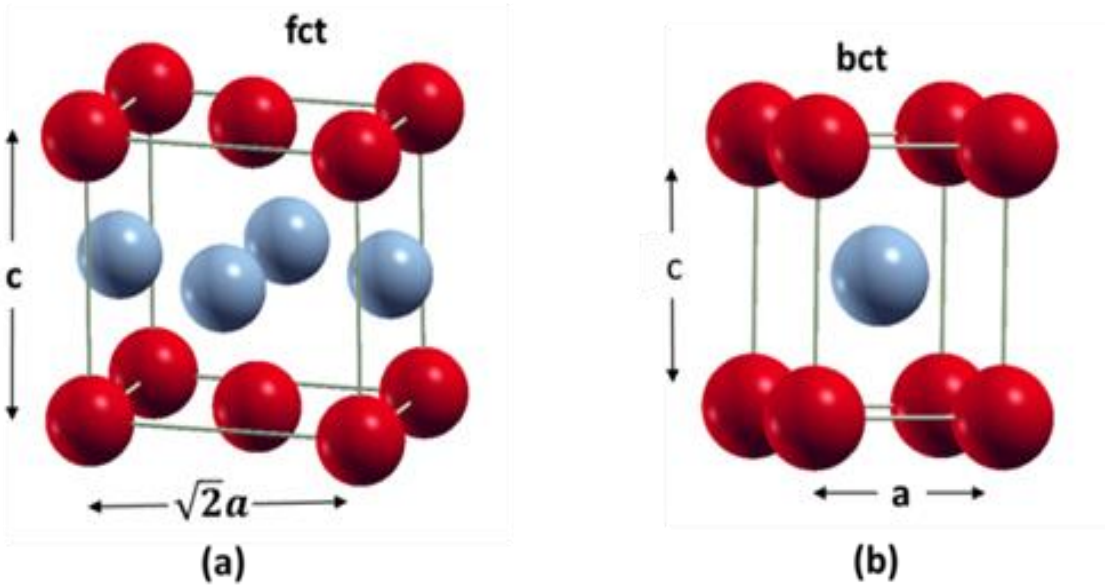

Figure (III.1): Crystal structure of the $L1_0$ phase of FeNi: (a) face-centered tetragonal and (b) body-centered tetragonal unit cells.

The c-axis is used to extend the layers (or z-axis).The reported theoretical value of the lattice parameters a is equal 2.53 Å and c is equal 3.58 Å, with a crystal structure belongs to the space group P4/mmm space group [15]. Figure (III.2) shown unit cell of tetrataenite $L1_0$-FeNi.

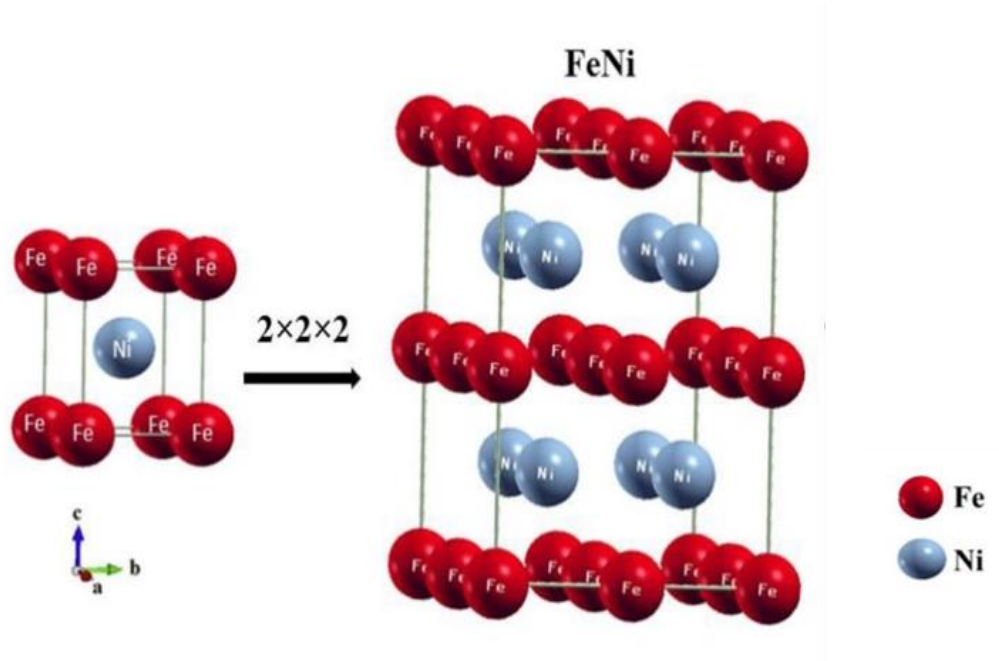

Figure (III.2): Unit cell of tetrataenite $L1_0$-FeNi.

Our approach begins with structural optimization, or figuring out the equilibrium parameters of compounds, which serves as the foundation for the remaining computations. A and c (Å), volume V_0 (in $Å^3$), bulk modulus B_0 (GPa), first pressure derivative B', and minimum total energy E_0 (eV) are examples of equilibrium lattice characteristics that are important in defining how responsive and stable the crystal structure is under various circumstances. Therefore, by fitting the curves of total energy minimization using the Murnaghan equation of state that is given by [16]

$$E(V) = E_0 + \frac{B_0}{B\prime(B\prime-1)}\left[V\left(\frac{V_0}{V}\right)^{B\prime} - V_0\right] + \frac{B_0}{B\prime}(V - V_0) \qquad \text{(III.7)}$$

Where B_0 is the bulk modulus, B_0' is its derivative, V is the strained volume, E_0 is the minimum energy, and V_0 is the reference volume.

The equilibrium lattice constants, equilibrium volume V_0 , equilibrium volume coefficients B_0, and first pressure derivative for volume units B_0' can all be found. Until the required convergence is attained, the optimization cycle is repeated. The total energy is shown in Figure (III.3) as a function of both volume and c/a volume.

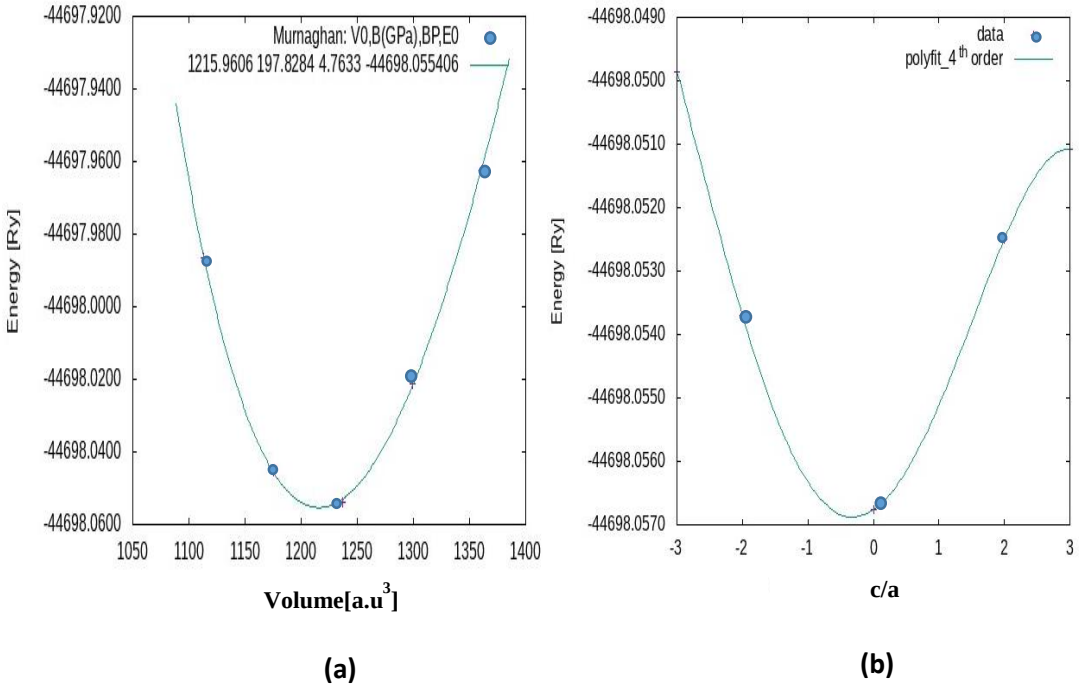

Figure (III.3): (a) Total energy vs the volume and (b) total energy as a function of c/a ratio of the $L1_0$-FeNi compound.

Further, to examine the stability of the structure, the formation energy (E_{for}) of L10-FeNi alloy was estimated using the prescribed formulae [17]:

$$E_{for}^{FeNi} = E_{FeNi} - E_{Fe} - E_{Ni} \quad \text{(III.8)}$$

Where E_{FeNi}, E_{Fe}, and E_{Ni} stand for the ground state energies of individual Fe and Ni atoms as well as pure FeNi supercells.

Table (III.1) illustrates the calculated ground state parameters, formation energy (E_F) as well as the available experimental and theoretical data.

Our calculated lattice parameters for $L1_0$-FeNi agree with experimental findings (a = 2.533 and c = 3.582) [18, 19] and also with the previous calculations for tetragonally ordered FeNi (a = 2.531 Å to a=2.58 and c = 3.579 Å to c=413) [17, 20]. Furthermore, the calculation formation energy was found to be -0.181/f.u is consistent with previous results, and the negative value of formation energy (E_{For}) that was observed is indicative of structural stability.

The bulk modulus B_0 for the $L1_0$-FeNi was calculated to be 197.8 GPa at 0 K. Previous calculations using coherent potential approximation (CPA) of the $Fe_{0.5}Ni_{0.5}$ random alloy yielded a B_0 value of around 220 GPa. For contrast, the experimental B_0 values for the $Fe_{0.5}Ni_{0.5}$ alloy evaluated at room temperature range from 165 to 177 GPa [21], whereas the experimental B_0 values for Fe and Ni are about 170 and 180 GPa, respectively.

Table (III.1): The optimized lattice parameters (a and c), tetragonal distortion (c/a), formation energy, E_{For}/f.u. (eV), the bulk modulus B (GPa) and first order derivative of bulk modulus (B_0') of FeNi compound.

Compound	**Properties**	**This work**	**Experiment**	**Theory**	
$L1_0$-FeNi	a (Å)	2.514	2.53[18,19]	2.531 [17]	2.58 [20]
	c (Å)	3.562	3.58[18,19]	3.579 [17]	3.413 [20]
	c/a	1.417	1.415[18,19]	1.414 [17]	1.32 [20]
	V(Å^3)	22.52	22.91[18,19]	22.93 [17]	22.72 [20]
	B(GPa)	197.828	165-177[21]	194.0 [17]	177.8 [20]
	B'$_0$	4.763	/	/	4.98 [20]
	E_{For}/f.u	-0.181	/	-0.18 [17]	

III.3-2 Electronic properties:

Understanding the ground-state band structure is essential for comprehending the microscopic behavior of electrons in materials [22]. It gives a clue as to whether a material possesses metallic characteristics. The band structure of FeNi near the Brillouin zone's high symmetry point is shown in Figure (III.4). (R—Γ—X—M—Γ). The virgin $L1_0$-FeNi alloy's strong ferromagnetic character is highlighted by the spin-resolved band structure, which shows a clear separation between spin-up and spin-down bands close to the Fermi level. A number of bands in the spin-up channel cross the Fermi level, suggesting strong metallic behavior and high electron mobility, both of which improve the conductivity of the material. Although the spin-down channel exhibits metallic properties, ferromagnetic exchange splitting is shown by its bands being pushed to higher energy in comparison to the spin-up channel. The strong exchange interaction between the Fe and Ni atoms causes an upward shift of spin-down states, which strengthens the magnetic characteristics of the system [23]. The spin-up channel has a larger net magnetic moment than the spin-down channel because it has more states surrounding the Fermi energy (E_F). At the Fermi level, some bands show low dispersion, especially in the vicinity of the M-point. These flat bands play an important role in the system's magnetic moment and are linked to localized Fe 3d states.

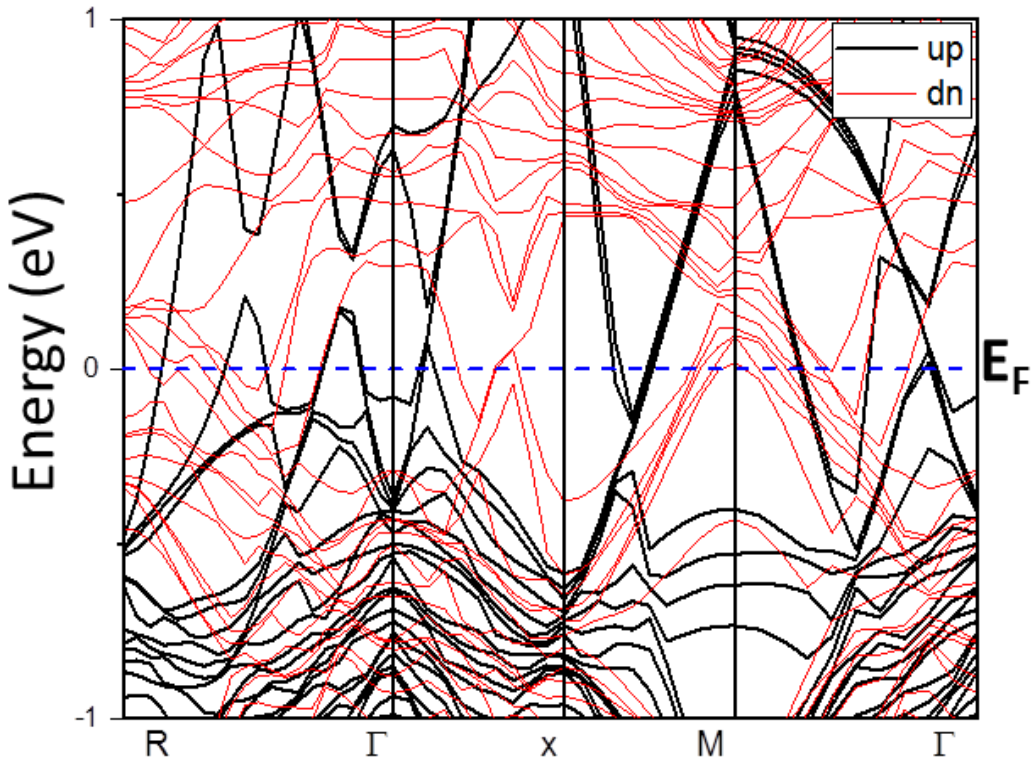

Figure (III.4): Energy band structure of $L1_0$-FeNi.

Figure (III.5) displays the total and orbital projected density of states (DOS) for $L1_0$-FeNi in order to examine the electronic characteristics. With the Fermi level set at zero, the positive values represent the spin-up density of states (DOS) and the negative values represent the spin-down states of DOS, with the Fermi level set at zero.

The distribution of electrons or holes among the accessible quantum states per unit volume at different energy levels is explained by the density of states. A significant number of quantum states that are open for electron or hole occupation are indicated by a high density of states at a certain energy level. On the other hand, a zero density of states, means that there are no accessible quantum states at that specific energy level [19].

It is evident from the (top panel) that $L1_0$-FeNi demonstrates pronounced magnetic properties, which can be ascribed to the significant asymmetry between the spin-up and spin-down total density of states (TDOS). Therefore, the total density of states (DOS) analysis confirms that the $L1_0$-FeNi alloy is spin-polarized, highlighting its ferromagnetic characteristics. The fundamental electronic configurations of the elements forming tetrataenite $L1_0$-FeNi are Fe: [Ar] $4s^2$ $3d^6$ and Ni: [Ar] $4s^2$ $3d^8$. The partial density of states (PDOS) reveals that Fe-3d and Ni-3d completely hybridize and contribute equally to the total DOS.

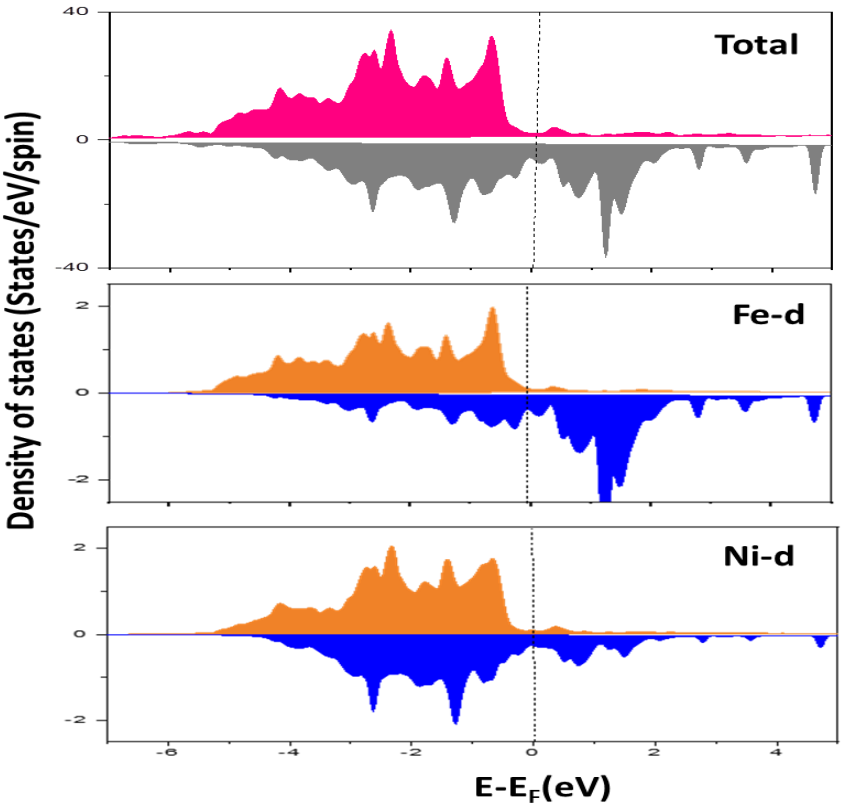

Figure (III.5): Computed total and projected density of states (DOS) for $L1_0$-FeNi alloy.

All alloys exhibit significant ferromagnetism due to the fact that the fully filled 3d-orbitals of Ni and Fe are easily identifiable in majority spin states whereas they are only partially occupied in minority spin states.

III.3-3 Magnetic properties:

The saturation magnetization (M_s) and total atom-resolved spin magnetic moments for the L_{10}-FeNi alloy are shown in Table (III.2). Analysis of the results shows that the estimated total and atom-resolved spin is quite similar to the measured results for the $L1_0$-FeNi phase both theoretically and experimentally [24,25]. The net magnetic moment is determined by the difference between majority and minority spin states in the region being occupied.

Table (III.2): Total and atom-resolved spin magnetic moments (μ_B), and saturation magnetization M_s (T) of $L1_0$- FeNi compound.

Compound	**Magnetic Moments(μ_B)**			**M_s (T)**
	Fe	**Ni**	**Total**	
FeNi (GGA)	2.702	0.651	3.265	1.32
FeNi (GGA+U)	2.658	0.678	3.271	
Ref. [24]	2.540	0.730		1.47
Ref. [25]	2.701	0.645	3.272	1.33

As seen in Figure (III.4), the minority spin states are less filled in Fe-3d as compared to Ni-3d, contributing large spin magnetic moments for Fe (2.702 μ_B) as compared to Ni (0.65 μ_B). The saturation magnetization (M_s) is determined as the total magnetic moment per volume. As shown in Table 2, the saturation magnetization of pristine FeNi is 1.32 T, which is nearly identical to the previously calculated theoretical value of 1.33 T [25, 26].

III.3-4 Thermodynamic properties:

One essential property for assessing the thermal stability of an alloy is its volumetric thermal expansion coefficient. Figure (III.6) displays the volumetric thermal expansion coefficient vs. temperature at various pressures for L_{10}-FeNi alloy. It is observed that the expansion coefficients increase slowly (almost linear increases) in the high-temperature region (up to 300 K) and exponentially in the low-temperature zone (T < 300 K). Our results are more in line with theoretical results when we compare the computed coefficient of thermal expansion of $L1_0$-FeNi to theoretical data [12].

As shown in Figure (III.6), the volumetric thermal expansion coefficient decreases with increasing pressure. This indicates that pressure has a significant impact on the coefficient at low pressure; however, this influence diminishes at higher pressures. According to the study, temperature and pressure both have an impact on the volumetric thermal expansion coefficient, and rising temperatures may counteract rising pressures.

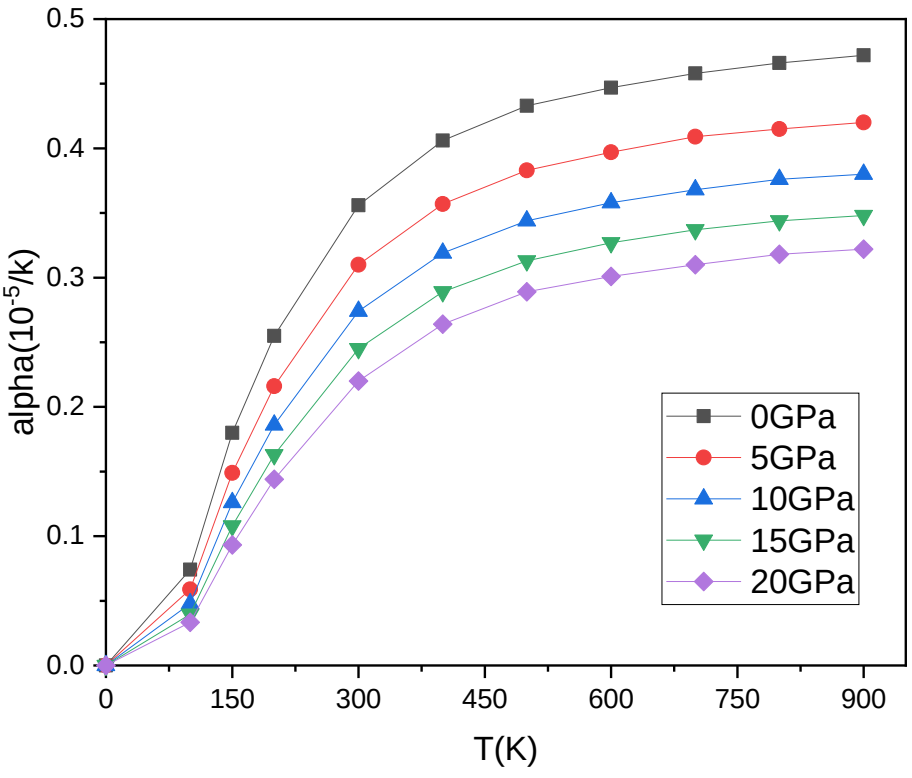

Figure (III.6): Volumetric thermal expansion coefficient versus temperature at different pressures of $L1_0$-FeNi alloy.

Also, the current computations support the Debye model. Both the force of atom-to-atom interaction and the melting point of compounds are related to the Debye temperature. with an increase in the Debye temperature, the melting point and contact force also rise. Figure (III.7) depicts the Debye temperature versus temperature for different pressures for $L1_0$-FeNi compound.

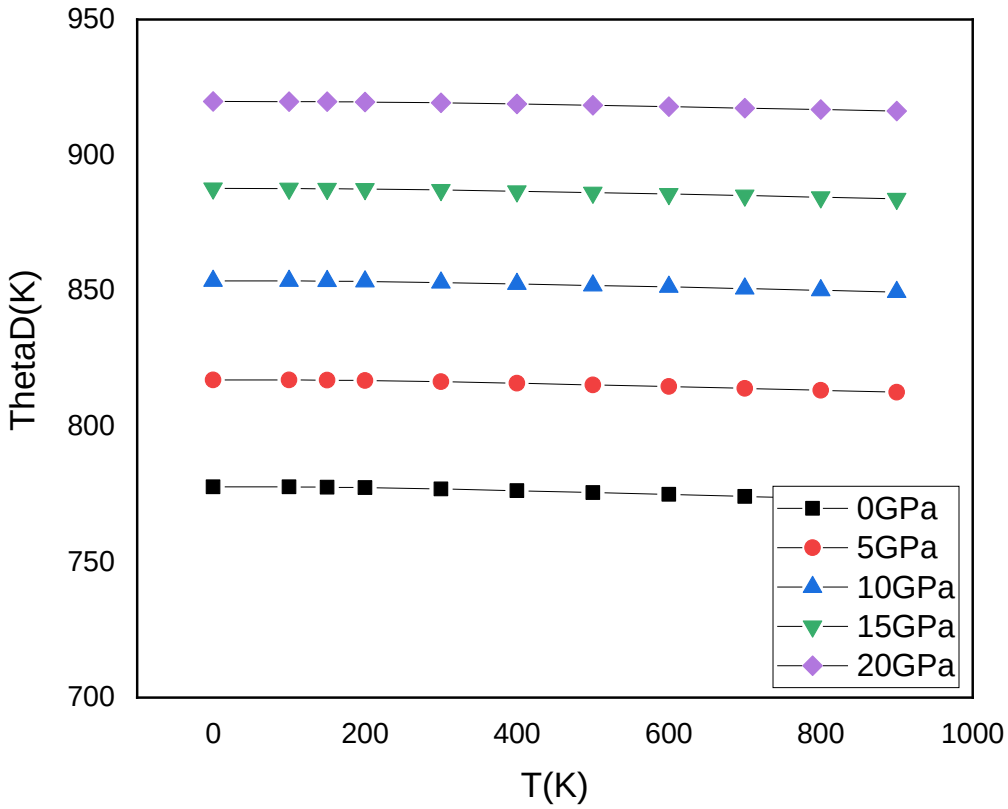

Figure (III.7): Debye temperature versus temperature at different pressures of $L1_0$-FeNi alloy.

$L1_0$-FeNi's greater Debye temperature indicates that these compounds are thermally stable, which makes them excellent thermal conductors by enabling electrons to flow across lattice planes with less scattering (low electron-phonon coupling) [27]. It is clear that, of all the temperatures, the L_{10}-FeNi alloy at 20GPa has the highest Debye temperature. This suggests that this alloy has the highest thermal stability and melting points across a range of temperatures.

Furthermore, one important indicator of an alloy's thermal stability is its constant volume heat capacity. The $L1_0$-FeNi alloy's constant volume heat capacity at different pressures and temperatures is shown in Figure (III.8).

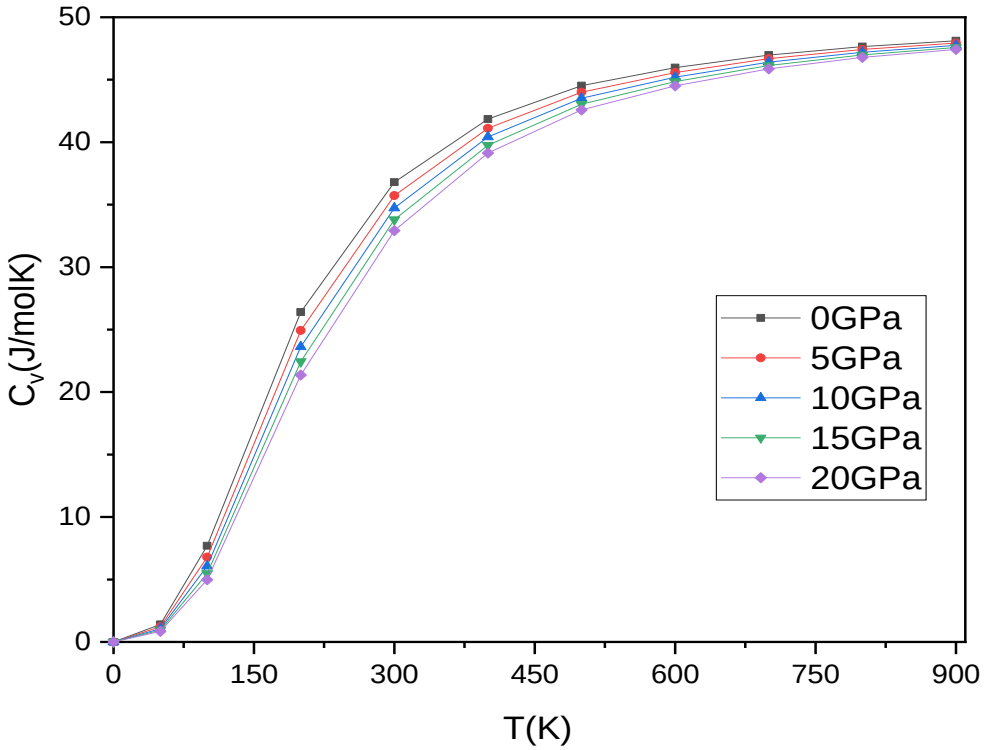

Figure (III.8): Constant volume heat capacity versus temperature at different pressures of $L1_0$-FeNi alloy.

As demonstrated in Fig. (III.8), when the temperature is less than 500 K, the constant volume heat capacity of the $L1_0$-FeNi alloy increases significantly at various pressures. However, at temperatures over 500 K, the constant volume heat capacity of this alloy approaches the Dulong-Petit limit (about 99.77 J.mol^{-1}. K^{-1}) [28]. Figure (III.8) shows that C_V decreases as pressure increases. Similarly to the previous comments regarding thermal expansion, the impact of pressure on the C_V is greatest at low pressure and gradually diminishes as pressure increases. It has been found that temperature affects C_V more than pressure does.

III.4- Study of structural, electronic, magnetic, and thermodynamic of Cobalt doping the L10-FeNi alloy.

III.4-1 Structural properties:

The 12.5% Co substitution process was started by substituting a Co atom for a Ni(Fe) atom using the internal structure of a 2x2x2 FeNi (bct) supercell (Fig. (III.2)) with a four-cell bct unit, as seen in Figure (III.9). Likewise, an 8.33% substitution ratio might be seen in a 2x2x3 supercell.

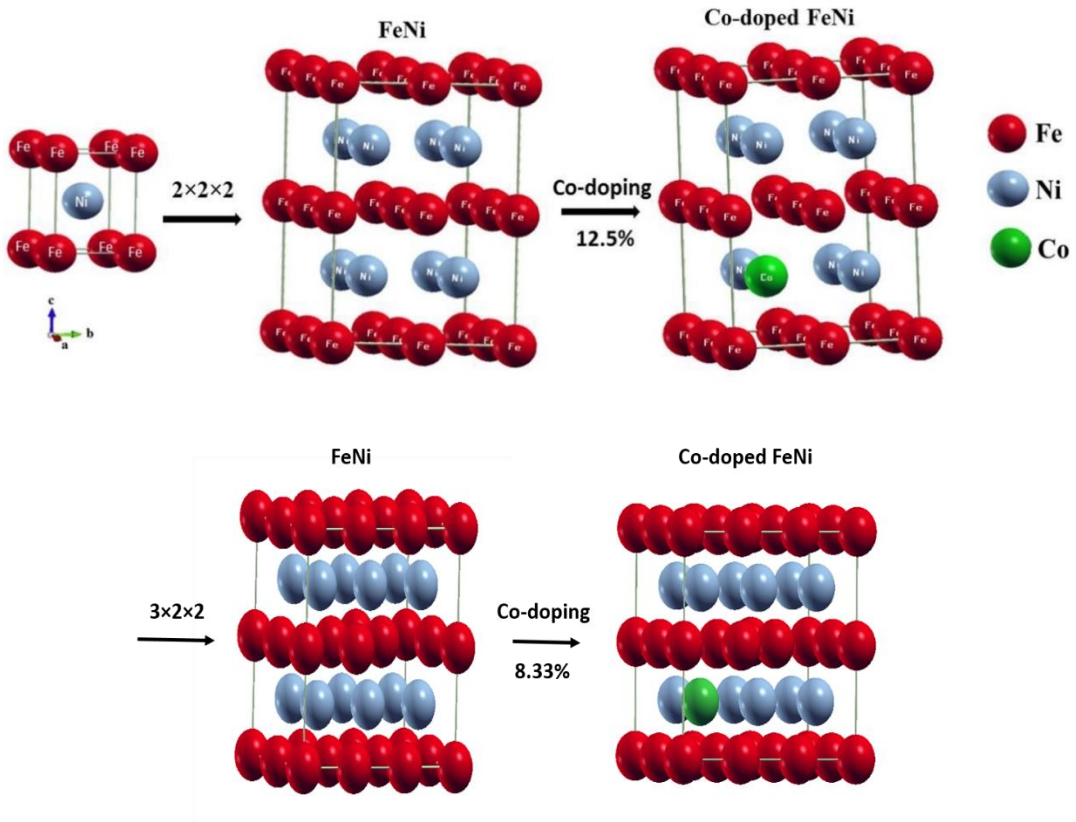

Figure (III.9): Schematics of 2 × 2 × 2 and 3×2×2 super cell of FeNi employed to simulate cobalt doping by replacing 12.5 % and 8.33% of the nickel atoms with cobalt.

We used the L. D. Marks [6] optimization approach to optimize the volume to find the lattice constants (a, b, c) of the $L1_0$-doped FeNi alloys in the ground state. As illustrated in Figure (III.10), we determined the lattice parameters, bulk modulus, and pressure derivative of the $Fe_{1-x}NiCo_x$ and $FeNi_{1-x}Co_x$ alloys by fitting the total energy versus volume data to the nonlinear Murnaghan equation of state [16]. Table (III.3) shows the collected results.

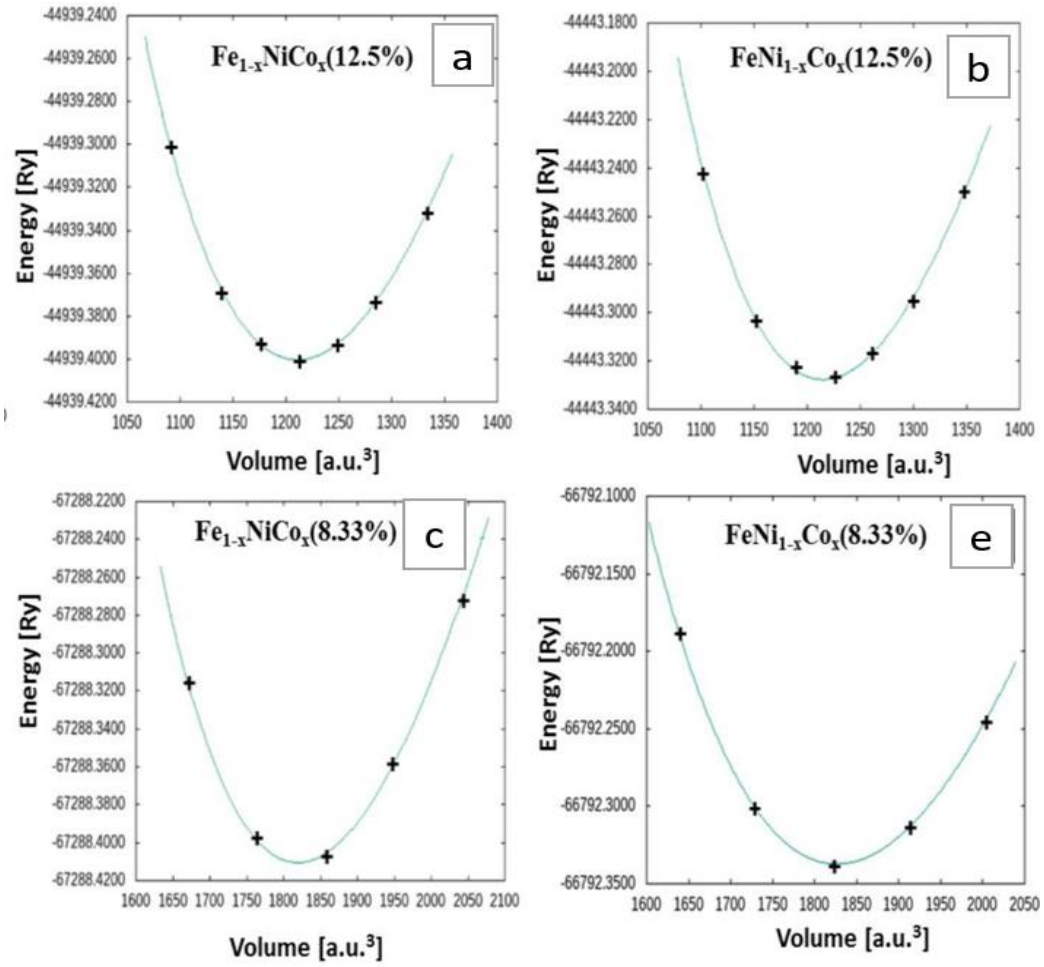

Figure (III.10): The total energy versus the volume for (a)$Fe_{1-x}NiCo_x$ (12.5%), (b)$FeNi_{1-x}Co_x$ (12.5%), (c) $Fe_{1-x}NiCo_x$ (8.33%), and (d)$FeNi_{1-x}Co_x$ (8.33%) alloys.

First, using the specified formulas, the formation energy (E_{for}) of FeNi:Co has been calculated in order to evaluate the stability of the structure [17]:

$$E_{for}^{FeNi-Co} = (E_{FeNi-Co} - xE_{Fe} - yE_{Ni} - zE_{Co}) \qquad \text{(III. 9)}$$

In this context, $E_{FeNi\text{-}Co}$, E_{Fe}, E_{Ni}, and E_{Co} represent the ground state energies of pure $Fe_{Ni\text{-}Co}$ supercells, as well as the individual energies of Fe, Ni, and Co atoms. The variables x, y, and z indicate the number of Fe, Ni, and Co atoms in the corresponding supercell. The formation energies (E_{for}) of the Co-doped FeNi alloy per formula unit have been calculated and are presented in Table (III.3).

Table (III.3): The optimized lattice parameters a and c (Å), tetragonal distortion (c/a), formation energy E_{For}/f.u. (eV), the bulk modulus B (GPa) and first order derivative of bulk modulus (B_0') of FeNi:Co compounds.

Compound	Supercell	a (Å)	c (Å)	c/a	V(Å^3)	B(GPa)	B_0'	E_{for}
FeNi (This work)	2 × 2 × 2	2.514	3.562	1.417	22.51	197.828	4.763	-0.181
Exp. [29]		2.533	3.582	1.414	22.98			
Theor. [17]	2 x 2 x 2	2.531	3.579	1.414	22.93			-0.18
$Fe_{1-x}NiCo_x$(12.5%)	2 × 2 × 2	2.515	3.577	1.422	22.62	199.617	4.959	-0.26
$FeNi_{1-x}Co_x$ (12.5%)	2 × 2 × 2	2.516	3.567	1.418	22.58	196.776	5.430	-0.23
$Fe_{1-x}NiCo_x$ (8.33%)	3 × 2 × 2	2.515	3.573	1.421	22.60	191.279	5.137	-0.27
$FeNi_{1-x}Co_x$ (8.33%)	3 × 2 × 2	2.521	3.568	1.416	22.67	0187.35	4.34	-0.24
Theor. [30]								
$Fe_{1-x}NiCo_x$ (12.5%)	2 x 2 x 1	2.509	3.575	1.424	22.50			
$Fe_{1-x}NiCo_x$ (8.33%)		2.51	3.565	1.420	22.46			

The lattice parameters and c/a ratios for the $Fe_{1-x}Co_xNi$ alloy, with Co concentrations of 12.5% and 8.33%, show excellent agreement with the previously reported values by Islam and Borah (2021) [30]. When cobalt is added to the ONi or OFe sites and the structure is relaxed, the c/a ratio increases compared to the pure alloy. This increase is attributed to the tetragonal distortion induced by Co doping.

The reason for the rise in the c/a ratio is that the 3d-element Co is comparatively greater than the 3d-elements Fe and Ni. Additionally, the observed negative formation energy (E_{for}) values provide compelling evidence of improved structural stability across all examples studied, as they systematically drop with cobalt doping. Thus, the tetragonal distortion induced by Co doping contributes to the improved stability of the FeNi alloy. The differences in c/a ratios between the pure and doped compounds offer valuable insights into how substitution affects the overall crystal geometry and the structure of the materials.

III.4-2 The Electronic Properties:

III.4-2- 1. The Band Structure:

To investigate the electronic properties of Co-doped FeNi alloys, we analyze the band structure, as shown in Figures (III.11). This figure illustrates the spin-resolved band structure of Co-doped $L1_0$-FeNi alloys at varying concentrations of 12.5% and 8.33%. The spin-up bands are represented by (black lines), while the spin-down bands are shown in (red lines). These bands are plotted across high-symmetry points in the Brillouin zone, with the Fermi level (E_f) indicated at 0 eV by a (dashed blue line).

In the case of 12.5% cobalt in both substitution configurations (refer to Figures (III.11-a) and (III.11-b)), the Fermi energy shifts downward compared to the $L1_0$-FeNi alloy(Figure III.4), with a more pronounced effect observed in the spin-down channel. In the spin-up channel, many bands still cross the Fermi level; however, the density of states near this level decreases, indicating that there are fewer available conductive states. Conversely, in the spin-down channel, bands move closer to or cross the Fermi level, resulting in a more metallic character. This shift in Fermi energy is attributed to the electron contributions from cobalt ($3d^74s^2$), which redistribute the electronic states and lead to a downward shift in the Fermi level.

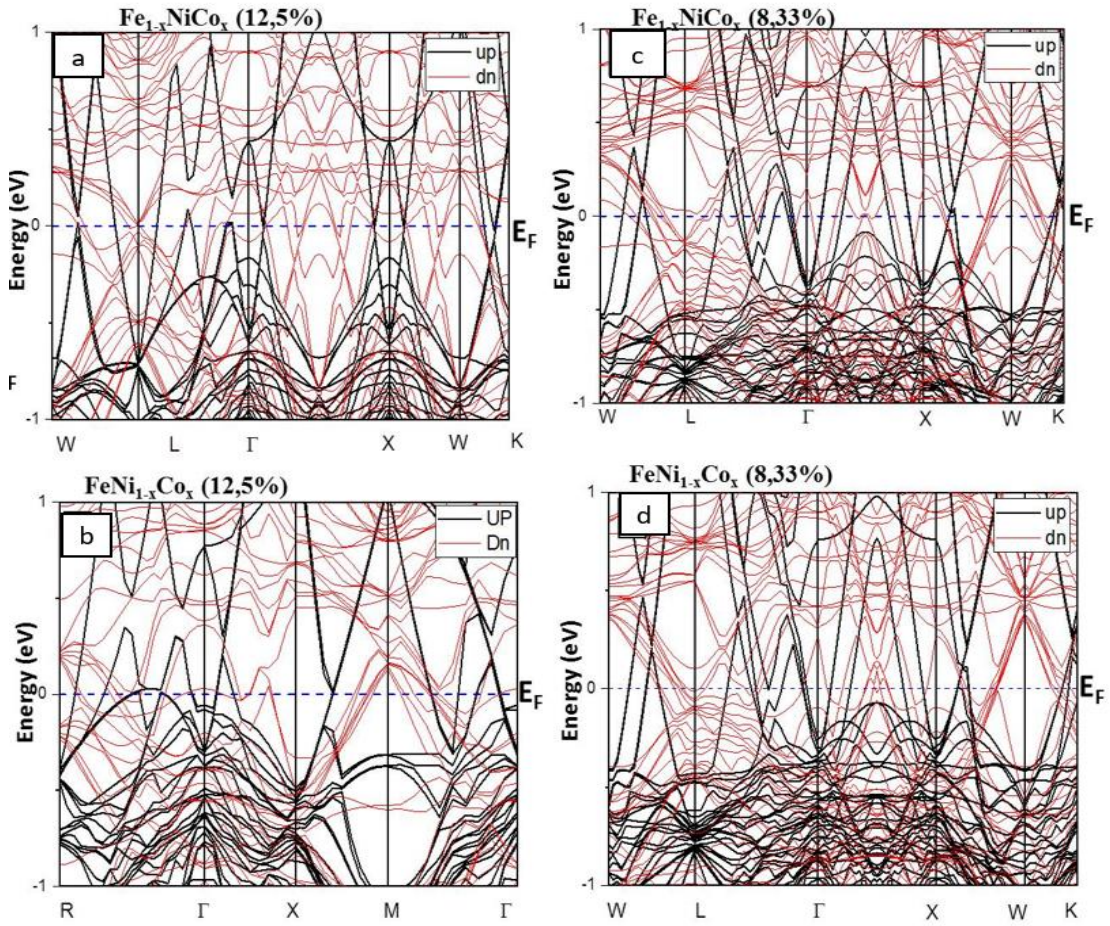

Figure (III.11): Energy band structure curves of (a) Fe1-xNiCox (12.5%), (b) FeNi1-xCox (12.5%), (c) Fe1-xNiCox (8.33%) ,and (d) FeNi1-xCox (8.33%).

Consequently, both spin channels contribute more equally to electrical conduction. This reduction in spin asymmetry is crucial for applications like spintronics, where a strong spin polarization is typically required [31]. Additionally, Both the spin-up and spin-down bands show a minor increase in dispersion, especially around the X and Γ points, as shown in Figure (III.11-c). More electron mobility within both spin channels is suggested by this improved dispersion, which could have a favorable effect on electronic conductivity.

At a cobalt concentration of 8.33%, in both substitution configurations, the Fermi energy shifts downward compared to pure FeNi (as shown in Figures (III.11-c) and (III.11-d)). However, this change is less significant than at a concentration of 12.5% cobalt, indicating that the electron redistribution is smaller than in the 12.5% cobalt case. Even at 8.33% cobalt, the system demonstrates reduced spin asymmetry, with more minority states contributing to conduction. At lower cobalt levels, the electronic properties are more similar to those of pure FeNi, but the shift in the Fermi energy indicates that cobalt still affects the balance between up and down spin bands.

III.4-2 2. Density of States (DOS):

As illustrated in Figure (III.12), the total DOS attests to the fact that every alloy exhibits metallic properties and spin polarization. Figures (III.12-a) and (III.12-b) show that the substitution of 12.5% Co at both the Fe and Ni sites raises the DOS close to the Fermi level, suggesting a change in the electronic states brought about by the additional 3d states of Co that hybridize with Fe-d and Ni-d orbitals. Hybridization between Co, Fe, and Ni orbitals is revealed by the new Co-d DOS profile, which affects the ferromagnetic phase's stability and magnetic moment. Due to the higher exchange contacts made possible by the hybridized Fe-Co states, this interaction can improve magnetic coupling. While the Ni-d orbitals vary less than the Fe-d orbitals, Ni-Co hybridization close to the Fermi level improves the alloy's ferromagnetic properties.

In FeNi with 8.33% Co doping, as shown in Figure (III.12-d), the density of states (DOS) indicates an increased spin asymmetry near the Fermi level. This implies stronger ferromagnetic interactions and increased spin polarization. Below the Fermi level, the spin-polarized regions are dominated by Fe and Co states, while the contribution from Ni decreases, indicating a shift in electron density towards the Fe and Co. Additionally, new Co (3d) states appear around the Fermi level, introducing spin-polarized states that align with the Fe and Ni (3d) states, thereby strengthening the alloy’s net magnetic moment through collective ferromagnetic coupling. With 8.33% Co doping, significant hybridization occurs between the 3d states of Fe, Ni, and Co, altering the bonding structure and enhancing exchange interactions.

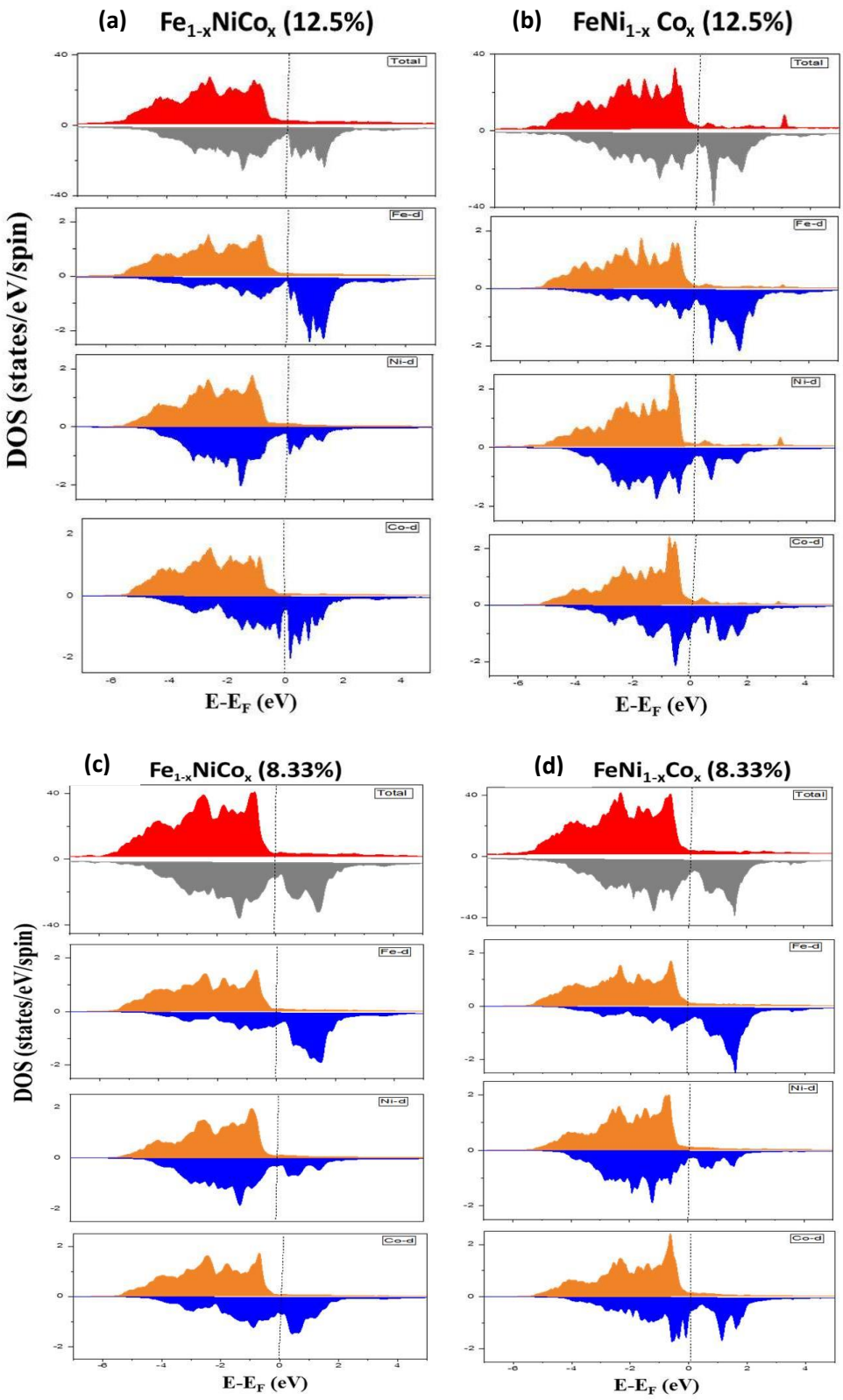

Figure (III.12): Computed total and projected density of states (DOS) for (a) Fe1-xNiCox (12.5%), (b) FeNi1-xCox (12.5%), (c) Fe1-xNiCox (8.3%) and (d) FeNi1-xCox (8.3%).

III.4-2 3. Charge Density Distribution :

The computed charge density distribution, which displays the type of chemical bonds present in $L1_0$-FeNi and Co-doped FeNi alloys, is displayed in Figure (III.13).

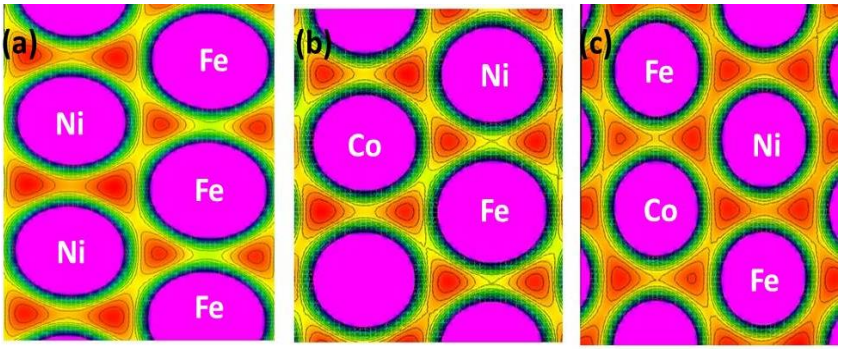

Figure (III.13): Contour maps of electron density distributions of (a) $L1_0$-FeNi, (b) $Fe_{1-x}NiCo_x$ (8.33%) and $FeNi_{1-x}Co_x$ (12.5%) alloys.

The charge density distribution of the pristine $L1_0$-FeNi alloy is shown in Figure (III.13-a). The consistent electron density distribution surrounding the Fe and Ni atomic centers in the $L1_0$-FeNi alloy suggests delocalized metallic bonding. Although there is minimal directed electron density, indicating weak covalent bonds, the predominant metallic bonding contributes to good electrical conductivity and mechanical properties.

Because of Co's unique electron configuration and stronger interaction with Fe, a minor portion of Fe is substituted by Co in Fe_{1-x} Ni Co_x with 8.33% see Figure (III.13-b), which helps to improve electron localization around the Co atoms. Co has more unpaired d-electrons than Ni, which allows for more d-orbital overlap between Co and Fe atoms. This results in an enhanced covalent character, especially in Fe-Co couples where the electron density is more concentrated along the bond lines. While metallic bonding is the main form of interaction, the introduction of Co changes the bonding characteristics by increasing the localized electron density between certain atomic pairs, especially between Fe-Co. This is demonstrated by the formation of slightly elongated or directional electron density, which indicates that covalent interactions are enhanced.

As shown in Figure (III.13-c), at higher Co concentrations (12.5%), the charge density around Co atoms in $FeNi_{1-x}Co_x$ alloy becomes more localized, especially near Fe and neighboring Ni atoms, indicating stronger covalent-like connections than at lower Co concentrations. Due to the overlap of the d orbital of Co and the slightly higher electronegativity of Ni, this higher Co content creates a marked directional electron density between the Fe-Co and Ni-Co pairs, indicating an enhanced covalent bond nature. The resulting structure exhibits a heterogeneous bonding pattern, with significant covalent properties localized around Co atoms, but overall it primarily demonstrates metallic bonding. Alloys with a higher Co concentration show a mixed bonding feature that enhances both mechanical and magnetic stability.

III.4-3 The magnetic properties:

The saturation magnetization (M_s) and the total atom-resolved spin magnetic moments for Co-doped FeNi are presented in Table (III.4). The analysis indicates that the introduction of cobalt affects both the total magnetic moment and the magnetic moments of individual atoms. The net magnetic moment is determined by the difference between the minority and majority spin states in the occupied region.

Table (III.4): Total and atom-resolved spin magnetic moments(μ_B), and saturation magnetization Ms (T) of pure and Co-doped FeNi.

Compound	**Magnetic Moments (μ_B)**				**M_s (T)**
	Fe	**Ni**	**Co**	**Total**	
FeNi (this work)	2.702	0.651	/	3.265	1.32
Exp. [26]	2.540	0.730	/		1.47
Theor. [25]	2.701	0.645	/	3.272	1.33
$Fe_{1-x}NiCo_x$(12.5%)	2.6938	0.6444	1.8097	3.1211	1.30
$FeNi_{1-x}Co_x$(12.5%)	2.6788	0.6360	1.8975	3.3114	1.36
$Fe_{1-x}NiCo_x$(8. 33%)	2.6830	0.6537	1.7675	3,1894	1.31
$FeNi_{1-x}Co_x$(8.33%)	2.6934	0.6758	1.6186	3.308	1.35

Table (III.4) shows that substituting Co into the FeNi alloy increases the overall spin magnetic moment for both doping ratios when compared to the pure FeNi alloy (Table (III.2)). This occurs because Co has a greater spin magnetic moment than Ni. Conversely, substituting Co into O_{Fe} decreases the overall spin magnetic moment for both doping percentages since Iron has a higher spin magnetic moment than Co. Similarly, a recent study indicates that replacing Fe with Pd reduces the total spin magnetic moment, while replacing Ni with Pd increases it in relation to the L10-FeNi alloy[17]. Additionally, the calculated spin magnetic moments are isotropic for all the compounds analyzed.

The saturation magnetization (M_s) is defined as the sum of the magnetic moments per unit volume. As shown in Table (III.4), adding a cobalt (Co) atom to $L1_0$-FeNi (O_{Ni}) increased the saturation magnetization for FeNi-Co by 12.5% (8.3%), raising it from 1.32 T to 1.36 T (or from 1.32 T to 1.35 T). This rise results from the Co atom's larger magnetic moment than that of Ni, which is found in the plane with magnetic Co impurities. Consequently, the improvement observed in M_s indicates that cobalt (Co) not only possesses a greater magnetic moment than nickel (Ni), but it also fortifies the exchange contacts present inside the crystalline lattice, potentially enabling increased magnetic moment alignment.

Nevertheless, Co-substitution at FeNi:Co(O_{Fe}) causes a slight decrease in FeNi magnetization from 1.32 T to 1.31 (1.30)T for FeNi-Co at 8.3% (12.5%). This is explained by the Co atom's smaller magnetic moment than Fe. Because Co atoms replace Fe atoms with larger magnetic moments, ferromagnetic exchange contacts become weaker, as seen by the slight drop in saturation magnetization (M_s). A slight decrease in M_s results from this substitution since it lowers the net magnetic moment per unit cell.

This shows that Co maintains substantial ferromagnetic coupling with Fe and Ni in the $L1_o$ structure, even though the fall in M_s is less significant than anticipated. This suggests that the tetragonal structure of the $L1_o$-FeNi alloy is resistant to Co substitution, maintaining magnetic order with little interference from M_s [32,26]. Consequently, FeNi:Co (O_{Ni}) seems to be a more promising substitute for permanent magnetic materials based on its magnetic properties. On the other hand, the reduction in M_s leads to softer magnetic behavior, making it suitable for applications that require frequent magnetic switching. Therefore, Thus, optimizing M_s through alloy design and doping is crucial for tailoring materials to meet specific technological requirements.

III.4-4 Thermodynamic properties:

A crucial factor in evaluating the thermal stability of an alloy is its volumetric thermal expansion coefficient. Figure (III.14) illustrates the relationship between the volumetric thermal expansion coefficient and temperature for the $Fe_{1-x}NiCo_x$ (12.5% and 8.33%) alloys, as well as for the $FeNi_{1-x}Co_x$ (12.5% and 8.33%) alloys at various pressures.

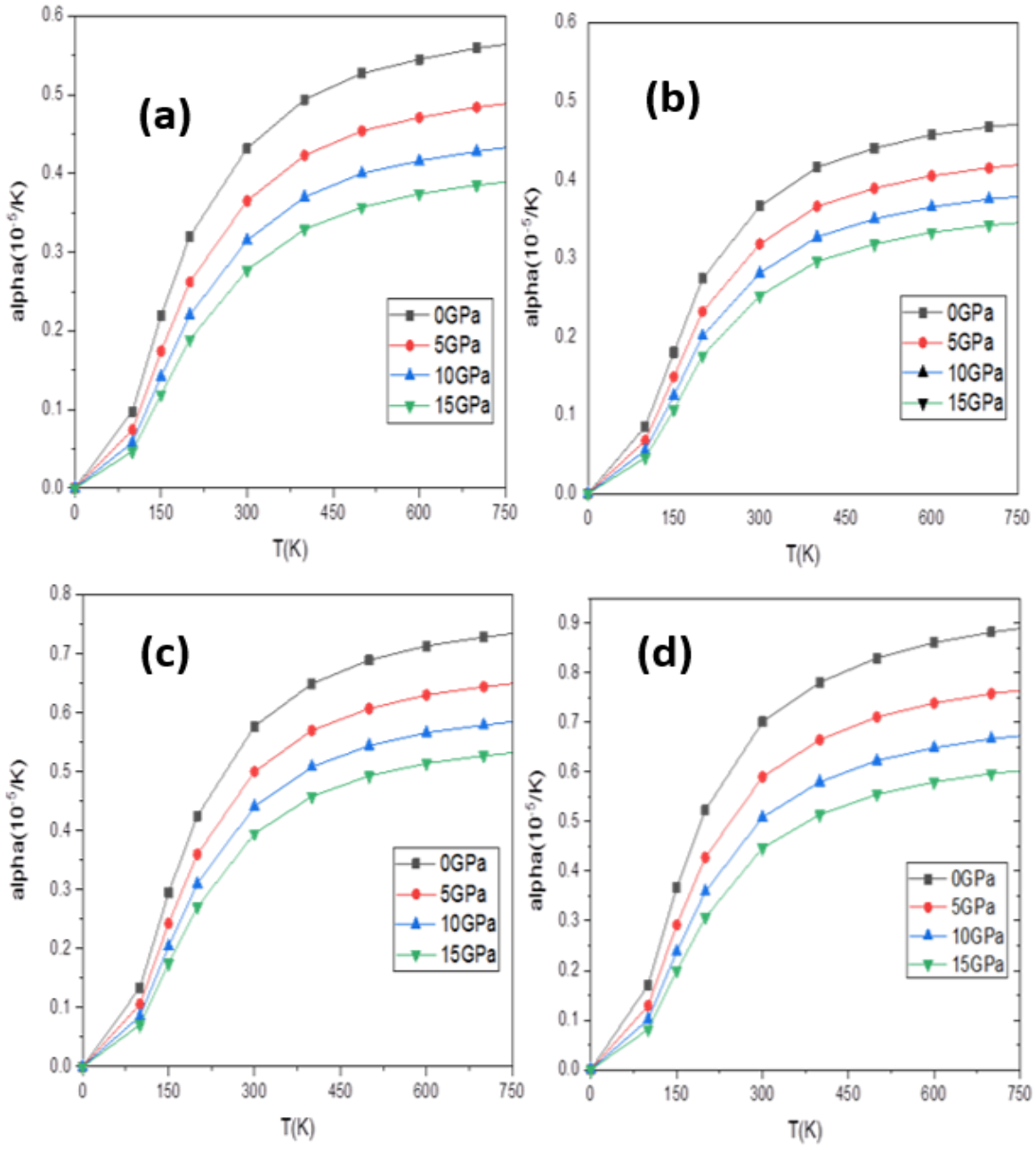

Figure (III.14): Volumetric thermal expansion coefficient versus temperature at different pressures for (a) $Fe_{1-x}NiCo_x$ (8.33%), (b) $FeNi_{1-x}Co_x$ (8.33%), (c) $Fe_{1-x}NiCo_x$ (12.5%) and (d) $FeNi_{1-x}Co_x$ (12.5%).

FeNi: Co(O_{Fe}) and FeNi: Co(O_{Ni}) alloys with a ratio of 8.33% consistently exhibited the lowest volumetric thermal expansion coefficient at the same temperature and pressure, indicating that these alloys are the most thermally stable. Our results thus show that lower cobalt doping rates can enhance the thermal stability of codoped FeNi alloys. Additionally, the $FeNi_{0.92}Co_{0.08}$ alloy continuously exhibits the lowest volumetric thermal expansion coefficient, proving that the alloy's thermal stability is improved by substituting Co for Ni.

Additionally, the Debye temperature is correlated with the melting point of compounds and the strength of interactions between atoms. As the Debye temperature increases, both the melting point and the interaction strength also rise. Figure (III.15) illustrates the relationship between Debye temperature and temperature at different Fe1-xNiCox (12.5% and 8.33%), and $FeNi_{1-x}Co_x$ (12.5% and 8.33%) compounds.

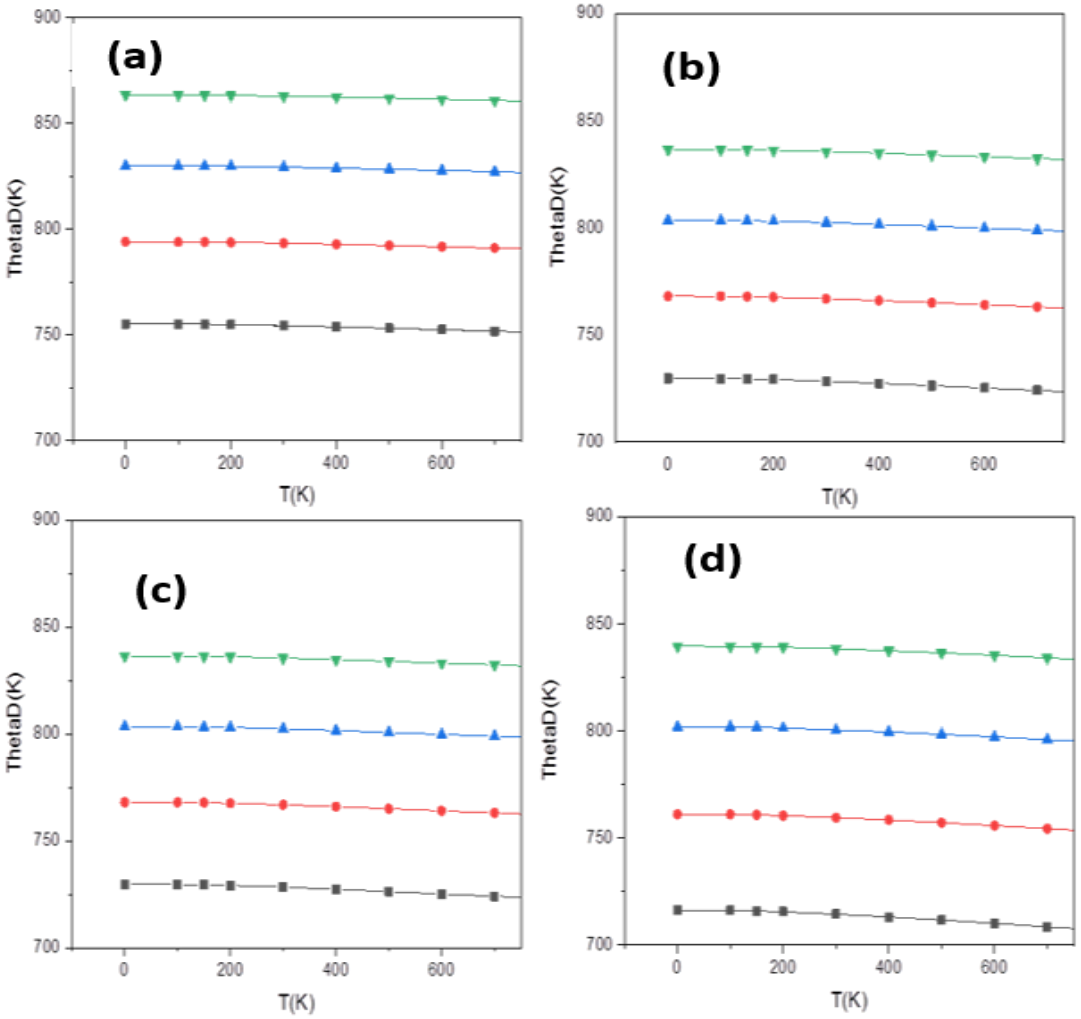

Figure (III.15): Debye temperature versus temperature at different pressures of: (a) Fe1-xNiCox (8.33%) (b) FeNi1-xCox (8.33%) (c) Fe1-xNiCox (12.5%) (d) FeNi1-xCox (12.5%).

The doped FeNi:Co(O_{Fe}) alloy, with an 8.33% concentration, consistently exhibits the highest Debye temperature across all temperatures. This indicates that this alloy is the most thermally stable and has the highest melting points at various pressures. However, in line with the observed pattern of bulk modulus changes, the Debye temperature of the Co-doped FeNi alloy decreases as the cobalt content increases.

Another important indicator of an alloy's thermal stability is its constant volume heat capacity. as illustrated in Figure (III.16) the constant volume heat capacity at various pressures and temperatures for Fe1-xNiCox (12.5 % and 8.33 %), and FeNi1-xCox (12.5 % and 8.33 %) compounds.

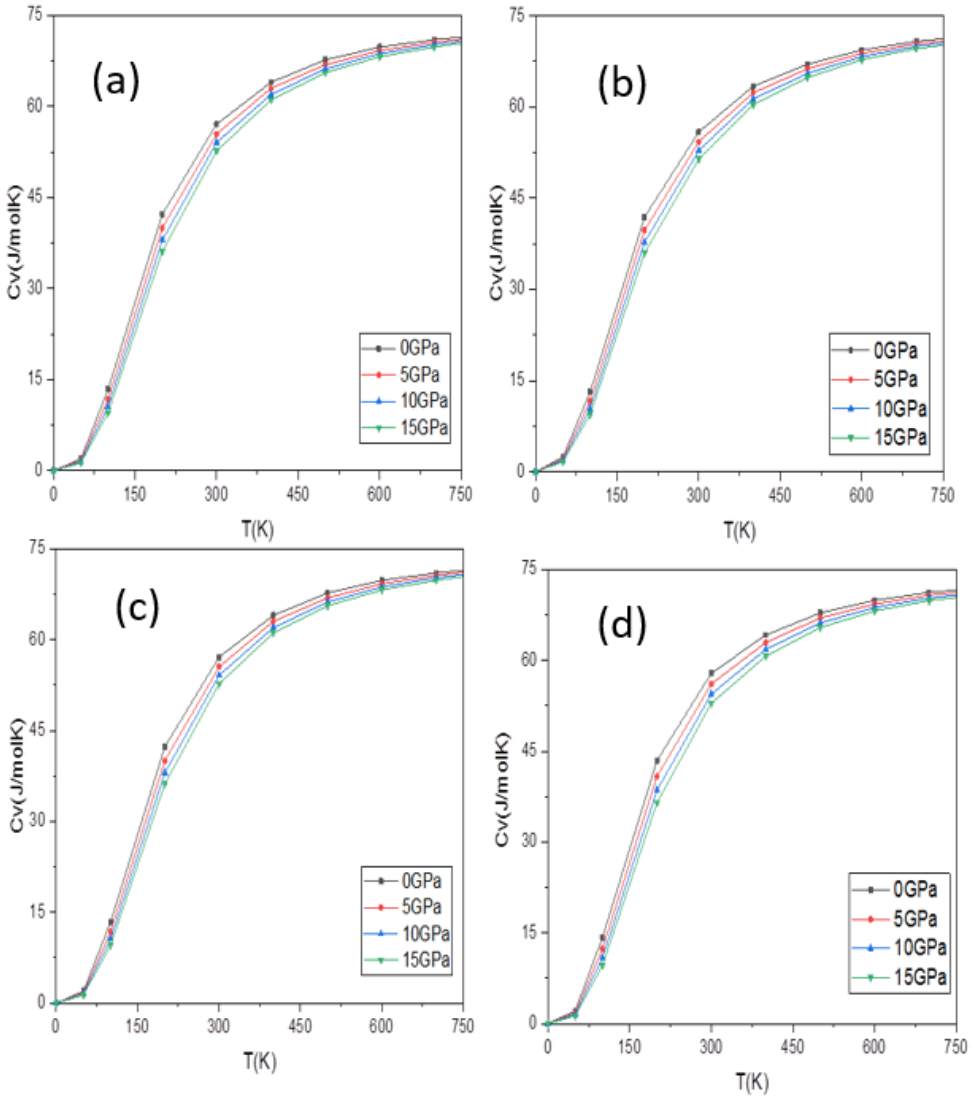

Figure (III.16): Constant volume heat capacity versus temperature at different pressures of: (a) $Fe_{1-x}NiCox$ (8.33%) (b) FeNi1-xCox (8.33%) (c) Fe1-xNiCox (12.5%) (d) FeNi1-xCox (12.5%).

The volume constant heat capacity of cobalt-doped FeNi alloys exceeds that of FeNi alloys when the temperature drops below 700 K (see Figure 8). Moreover, from a numerical perspective, the volume constant heat capacity of these four alloys differs very little, indicating that the volume constant heat capacity of cobalt-alloyed FeNi alloys is not significantly affected by the increase of cobalt concentration.

III.5 Comparison with Previous Doping Studies and Current Findings:

When comparing the results of this study to previous research, it is evident that cobalt doping offers distinct advantages due to cobalt's atomic size, which closely matches that of Fe. This similarity minimizes structural distortion within the $L1_0$-FeNi phase, thereby stabilizing the alloy, enhancing crystallinity, and maintaining structural symmetry without inducing lattice strain. In contrast, doping with Pt and Pd results in a slight increase in lattice constants with minimal distortion, contributing to stability. However, Pt doping is constrained by its high cost and significant weight, which limits its scalability in practical applications[15,17]. Meanwhile, N-interstitial doping introduces considerable tetragonal distortion to the $L1_0$-FeNi structure, improving the c/a ratio and magnetocrystalline anisotropy (MCA). Nonetheless, excessive distortion can lead to internal strain and lattice defects, which may undermine the alloy's long-term stability[20].

From an electronic and magnetic perspective, the doping elements significantly influence spin polarization and magnetic behavior in FeNi alloys. Cobalt doping, in particular, enhances spin polarization and magnetic exchange interactions, improving electronic stability while maintaining the robust ferromagnetic properties of $L1_0$-FeNi. Additionally, cobalt increases saturation magnetization due to its high magnetic moment and strong interaction with iron. These characteristics make Co-doped FeNi alloys well-suited for high-temperature applications where high magnetization and magnetic stability are critical.

FeNi alloys exhibit significant thermodynamic properties, including excellent phase stability and thermal resilience. Nitrogen doping contributes to stabilizing the L10 phase [33]; however, excessive concentrations may introduce strain, compromising long-term stability. Pt doping similarly enhances phase stability and maintains performance under elevated temperatures but is restricted in large-scale applications due to its high cost [17]. Boron doping effectively improves phase stability and high-temperature performance by mitigating grain growth. Notably, cobalt doping offers a comprehensive solution by ensuring both thermal and phase stability over a broad temperature range. These attributes position Co-doped FeNi alloys as an optimal choice for high-temperature and permanent magnet applications.

III.6 Conclusion:

The thorough examination of the L1₀-FeNi alloy highlights its unique magnetic characteristics and structural stability, which have been confirmed by both theoretical and experimental findings. The alloy's potential for a variety of uses is highlighted by its capacity to retain these qualities under a broad range of pressures and temperatures. The results revealed that cobalt (Co) doping significantly influences the structural, electronic, and magnetic properties of the L1₀-FeNi alloy.

Low Co concentrations were found to enhance structural stability, increase saturation magnetization, and improve thermal stability through a higher Debye temperature and a lower thermal expansion coefficient.ر These findings confirm that controlled doping is an effective strategy to tailor FeNi alloys for rare-earth-free permanent magnet applications.

References:

[1] Hirosawa, S., Nishino, M., & Miyashita, S. (2017). Perspectives for high-performance permanent magnets: applications, coercivity, and new materials. *Advances in Natural Sciences: Nanoscience and Nanotechnology*, *8*(1), 013002.

[2] Tian, L. Y., Levämäki, H., Eriksson, O., Kokko, K., Nagy, Á., Délczeg-Czirják, E. K., & Vitos, L. (2019). Density Functional Theory description of the order-disorder transformation in Fe-Ni. Scientific Reports, 9(1), 8172.

[3] Hlova, I. Z., Dolotko, O., Abramchuk, M., Biswas, A., Mudryk, Y., & Pecharsky, V. K. (2024). Enhancement of hard magnetism and chemical order of synthetic L10-FeNi. Journal of Alloys and Compounds, 981, 173619.

[4] Werwiński, M., & Marciniak, W. (2017). Ab initio study of magnetocrystalline anisotropy, magnetostriction, and Fermi surface of L10 FeNi (tetrataenite). Journal of Physics D: Applied Physics, 50(49), 495008.

[5] Makkar, P., & Ghosh, N. N. (2021). A review on the use of DFT for the prediction of the properties of nanomaterials. RSC advances, 11(45), 27897-27924.

[6] Blaha, P., Schwarz, K., Madsen, G. K., Kvasnicka, D., & Luitz, J. (2001). wien2k. An augmented plane wave+ local orbitals program for calculating crystal properties, 60(1).

[7]Perdew, J. P., Burke, K., & Ernzerhof, M. (1996). Generalized gradient approximation made simple. Physical review letters, 77(18), 3865.

[8] Blanco, M. A., Francisco, E., & Luana, V. G. I. B. B. S. (2004). GIBBS: isothermal-isobaric thermodynamics of solids from energy curves using a quasi-harmonic Debye model. Computer Physics Communications, 158(1), 57-72.

[9] Otero-de-la-Roza, A., & Luaña, V. (2011). Gibbs2: A new version of the quasi-harmonic model code. I. Robust treatment of the static data. Computer Physics Communications, 182(8), 1708-1720

[10] Blanco, M. A., Pendás, A. M., Francisco, E., Recio, J. M., & Franco, R. (1996). Thermodynamical properties of solids from microscopic theory: applications to MgF2 and Al2O3. Journal of Molecular Structure: THEOCHEM, 368, 245-255..

[11] Poirier, J. P. (2000). Introduction to the Physics of the Earth's Interior. Cambridge University Press.

[12] Zhang, J., Zhang, Y. P., & Su, C. M. (2020). First-principles study of FeNi1-xCrx ($0 \leq x \leq 1$) disordered alloys from special quasirandom structures. Calphad, 71, 102007.

[13] Francisco, E., Blanco, M. A., & Sanjurjo, G. (2001). Atomistic simulation of Sr F 2 polymorphs. Physical Review B, 63(9), 094107.

[14] Edström, A., Chico, J., Jakobsson, A., Bergman, A., & Rusz, J. (2014). Electronic structure and magnetic properties of L 1 0 binary alloys. Physical Review B, 90(1), 014402.

[15] Rani, P., Singla, R., Thakur, J., Reshak, A. H., & Kashyap, M. K. (2021). Enhancement in magnetic parameters of L1 0-FeNi on Pd-substitution for permanent magnets. Indian Journal of Physics, 1-6.

[16] Murnaghan, F. D. (1944). The compressibility of media under extreme pressures. Proceedings of the National Academy of Sciences, 30(9), 244-247.

[17] Rani, P., Thakur, J., Taya, A., & Kashyap, M. K. (2019). Magnetocrystalline anisotropy of Pt-doped L10-FeNi compound for clean energy applications. Vacuum, 159, 186-190.

[18] Lee, S., Edalati, K., Iwaoka, H., Horita, Z., Ohtsuki, T., Ohkochi, T., ... & Takanashi, K. (2014). Formation of FeNi with L 10-ordered structure using high-pressure torsion. Philosophical magazine letters, 94(10), 639-646.

[19] Geng, Y., Ablekim, T., Koten, M. A., Weber, M., Lynn, K., & Shield, J. E. (2015). Defect generation and analysis in mechanically alloyed stoichiometric Fe–Ni alloys. Journal of Alloys and Compounds, 633, 250-255.

[20] Pandya, N. Y., Mevada, A. D., & Gajjar, P. N. (2016). Effect of Temperature/Pressure on Lattice Dynamics of FeNi. Advanced Materials Research, 1141, 84-90.

[21] Aledealat, K., Aladerah, B., Obeidat, A., & Gharaibeh, M. (2021). First-principles study of electronic structure and magnetic properties of L10-ordered FeNi, FePd, and FePt alloys. Heliyon, 7(12).

[22] Marzari, N., Ferretti, A., & Wolverton, C. (2021). Electronic-structure methods for materials design. Nature materials, 20(6), 736-749.

[23] Wu, R., & Freeman, A. J. (1992). Structural and magnetic properties of Fe/Ni (111). Physical Review B, 45(13), 7205.

[24] Kotsugi, M., Mizuguchi, M., Sekiya, S., Mizumaki, M., Kojima, T., Nakamura, T., ... & Watanabe, Y. (2013). Origin of strong magnetic anisotropy in L10-FeNi probed by angular-dependent magnetic circular dichroism. Journal of magnetism and magnetic materials, 326, 235-239.

[25] Rani, P., Thakur, J., Taya, A., & Kashyap, M. K. (2019, July). Effect of tetragonal distortion induced by interstitial C-doping in L10-FeNi. In AIP Conference Proceedings (Vol. 2115, No. 1). AIP Publishing.

[26] Poirier, E., Pinkerton, F. E., Kubic, R., Mishra, R. K., Bordeaux, N., Mubarok, A., ... & Barmak, K. (2015). Intrinsic magnetic properties of L1 FeNi obtained from meteorite NWA 6259. Journal of Applied Physics, 117(17).

[27] Pandya, N. Y., Mevada, A. D., & Gajjar, P. N. (2016). Lattice dynamical and thermodynamic properties of FeNi3, FeNi and Fe3Ni invar materials. Computational Materials Science, 123, 287-295.

[28] Feldhoff, A. (2022). On the thermal capacity of solids. Entropy, 24(4), 479.

[29] Clarke, R. S., & Scott, E. R. (1980). Tetrataenite—ordered FeNi, a new mineral in meteorites. American Mineralogist, 65(7-8), 624-630.

[30] Islam, R., & Borah, J. P. (2021). Large magnetic anisotropy in Co–Fe–Ni–N ordered structures: a first-principles study. *Journal of Physics: Condensed Matter*, *34*(9), 095503.

[31] Hirohata, A., Yamada, K., Nakatani, Y., Prejbeanu, I. L., Diény, B., Pirro, P., & Hillebrands, B. (2020). Review on spintronics: Principles and device applications. *Journal of Magnetism and Magnetic Materials*, *509*, 166711.

[32] Cable, J. W., & Wollan, E. O. (1973). Magnetic-moment distribution in NiFe and AuFe alloys. *Physical Review B*, *7*(5), 2005.

[33] Rani, P., Kashyap, M. K., Singla, R., Thakur, J., & Reshak, A. H. (2020). Magnetism and magnetocrystalline anisotropy of tetragonally distorted L10-FeNi: N alloy. *Journal of Alloys and Compounds*, *835*, 155325.

General conclusion

General conclusion

This study provides valuable insights into the potential of cobalt-doped $L1_0$ and $L1_0$-FeNi nickel-iron alloys as promising alternatives to rare-earth-based permanent magnets, which are essential in various industrial and technological applications. Through the use of a linearized augmented plane wave approach, incorporating density functional theory and the generalized gradient approximation (GGA), we conducted a thorough investigation into their structural, electronic, magnetic, and thermodynamic properties. his study examined two types of co-substitution doping (O_{Ni}/O_{Fe}) at the nickel/iron site in the parent alloy, considering two different ratios. Additionally, a semi-harmonic Debye model, implemented using the Gibbs2 computational program, was utilized to analyze the thermodynamic properties of the alloys.

The structural analysis confirmed that the unique tetragonal configuration of $L1_0$-FeNi plays a crucial role in its exceptional magnetic properties. Furthermore, the introduction of cobalt at different substitution sites (O_{Ni}/O_{Fe}) within the parent alloy significantly affects its stability. The computed formation energy (Ef_{or}), elastic modulus (B0'), and lattice parameters were found to be consistent with previous theoretical and experimental results, further validating the structural integrity of these alloys. Additionally, it was observed that cobalt substitution induces a tetragonal distortion in the $L1_0$-BCT structure, leading to an increase in formation energy and enhancing the overall structural stability of the alloy.

From a magnetic perspective, the study demonstrated that the 3d orbitals of iron and nickel play a fundamental role in defining the metallic nature of these alloys. More importantly, the incorporation of cobalt into FeNi:Co(O_{Ni}) alloys was found to enhance key magnetic properties, including spontaneous magnetization and saturation magnetization (M_s), making them highly suitable for advanced magnetic applications.

The thermodynamic analysis further revealed that reducing the cobalt content in these alloys decreases the volumetric thermal expansion coefficient while simultaneously increasing the Debye temperature and strengthening interatomic interactions. This suggests that cobalt-doped $L1_0$-FeNi alloys not only exhibit improved thermal stability but also maintain desirable mechanical and electronic properties, making them robust candidates for high-performance permanent magnets.

In conclusion, this study enhances our understanding of the effects of elemental doping on the structural, electronic, magnetic, and thermodynamic characteristics of $L1_0$-FeNi alloys. The findings highlight their strong potential for rare-earth-free permanent magnet applications and pave the way for future research aimed at optimizing their performance for next-generation technological and industrial advancements.